

**February 2012
Ph.D. Dissertation**

**Development of analytical model for
Thermo-mechanical behavior of
dissimilar materials butt joint by TIG
Assisted Friction Stir Welding**

Graduate School of Chosun University

**Department of Naval Architecture and
Ocean Engineering**

M.S.Bijoy

Development of analytical model for Thermo-mechanical behavior of dissimilar materials butt joint by TIG Assisted Friction Stir Welding

TIG-FSW 하이브리드 용접을 이용한 이재접합부의
열기계적 거동에 대한 수학적 모델 개발

24th February 2012

Graduate School of Chosun University

**Department of Naval Architecture and
Ocean Engineering**

M.S.Bijoy

Development of analytical model for Thermo-mechanical behavior of dissimilar materials butt joint by TIG Assisted Friction Stir Welding

Advisor: Prof. Bang Han Sur

*This dissertation is submitted to the Graduate School of
Chosun University in partial fulfillment of the requirements
for the degree of Doctor of Philosophy in Engineering*

October 2011

Graduate School of Chosun University

**Department of Naval Architecture and
Ocean Engineering**

M.S.Bijoy

**This is to certify that the Ph.D. dissertation of M.S.Bijoy
has successfully met the dissertation requirements of
Chosun University.**

Department of Naval Architecture and Ocean Engineering,
Chosun University, Gwangju 501-759,
Republic of Korea.
Ph.D. Hee Seon Bang

Department of Naval Architecture and Ocean Engineering,
Chosun University, Gwangju 501-759,
Republic of Korea.
Ph.D. Han Sur Bang

Gyeongbuk Hybrid technology Institute
36 Goeyeon-Dong, Yeongcheon,
Gyeongbuk, 770-170, Korea.
Ph.D. Yong Gak Kweon

RIST welding research center,
San 32 Hyoja-Dong, Nam-gu, Pohang, Korea.
Ph.D. Woong Seong Chang

Automotive Components Center, Korea Institute of Industrial Technology
(KITECH), 1110-9 Oryong-dong,
Gwangju, 500-480, Korea
Ph.D. Ik Hyun Oh

December 2011

Graduate School of Chosun University

Contents

List of Tables.....	v
List of Figures.....	vi
Abstract (in Korean).....	x
Chapter 1 Introduction	1
1.1 Research Background	2
1.1.1 Research methodology	4
1.2 Literature review.....	5
1.2.1 Friction Stir welding	5
1.2.2 Phases of FSW process.....	6
1.2.3 TIG assisted FSW process	8
1.2.4 Characteristics of Base materials	9
1.2.5 Temperature dependent material properties of base materials	12
1.2.6 Thermal Modeling of Friction Stir Welding	14
Chapter 2 Analytical Model for dissimilar joint by TAFSW.....	19
2.1 Introduction.....	19

2.2 Tool geometry	19
2.3 Contact condition	20
2.4 Analytical estimation of heat generation	22
2.4.1 Heat generated at tapered pin surface	23
2.4.2 Heat input calculation for Preheating TIG Heat source	26
Chapter 3	
Heat Transfer and Residual Stress Analysis	27
3.1 Introduction.....	27
3.2 Theory of Numerical Simulation.....	32
3.2.1 Heat Conduction Analysis	32
3.2.2 Thermal elasto-plastic analysis	37
3.2.3 Temperature dependency of stress and strain	38
3.3 Data transferring between commercial software and - developed program.....	42
Chapter 4	
FEA and Experimental Method for TAFSW.....	45
4.1 Finite Element Analysis model.....	45
4.1.1 Coefficient of friction	47
4.2 Experimental method.....	48

4.2.1 Experimental measurement of temperature	52
4.2.2 Measurement of Residual stress	55
Chapter 5 Results and Discussions	57
5.1 Heat conduction analysis.....	57
5.1.1 Aluminum 6061-STS304 dissimilar butt joint	57
5.1.2 Aluminum 6061-SS400 dissimilar butt joint	62
5.2 Heat conduction analysis of TIG preheating.....	65
5.3 Analysis of dissimilar butt joint by Conventional FSW	
.....	67
5.4 Residual stress analysis.....	68
5.4.1 Al 6061-STS 304 dissimilar joint	70
5.4.2 Al 6061-SS400 dissimilar joint	74
5.5 Comparison of numerical simulated and -	
experimental result.....	78
Chapter 6	
Conclusion and future scope of work.....	82
6.1 Future scope of work.....	85
References	86
Abstract (in English).....	93

Acknowledgements.....	96
------------------------------	-----------

List of Tables

Table 1.1 Chemical composition and mechanical properties of Al 6061-T6	10
Table 1.2 Chemical composition and mechanical properties of STS304.....	11
Table 1.3 Chemical composition and mechanical properties of SS400.....	11
Table 2.1: Definition of contact condition related to tool and matrix velocity	22
Table 4.1 Coefficient of friction considered in various FSW numerical studies	47
Table 4.2 Temperature dependent friction coefficient of aluminum and steel	47
Table 4.3 Specification of tool used for TAFSW.....	48
Table 4.4 Optimum condition for TIG preheating	49
Table 4.5 Welding condition for TAFSW	49
Table 4.6 Residual stress values of dissimilar butt joint by TAFSW.....	56

List of Figures

Fig.1.1 Outline of Research methodology	4
Fig 1.2 Schematic of friction stir welding process	5
Fig 1.3 Plunging phase of FSW tool to work piece	6
Fig 1.4 Dwelling phase of FSW tool to work piece	7
Fig 1.5 Welding phase of FSW	7
Fig 1.6 Pulling out of FSW tool from work piece.....	8
Fig 1.7 Schematic of TIG assisted friction stir welding	9
Fig.1.8 Physical properties of Al-6061-T6	12
Fig.1.9 Mechanical properties of Al-6061-T6	12
Fig.1.10 Physical properties of STS304 and SS400	13
Fig.1.11 Mechanical properties of STS304 and SS400.....	13
Fig 2.1 Basic shape of the FSW tool assumed for analytical calculation	20
Fig 2.2 Heat generation contributions in analytical estimates	23
Fig 2.3 Schematic drawing of tool and infinitesimal segment area at pin surface	24
Fig 3.1 Flow diagram for heat conduction program	30
Fig 3.2 Flow diagram for Thermal-Elastic plastic analysis	32
Fig 3.3 Structure of the heat transfer analysis program	43
Fig 3.4 Structure of the residual stress analysis program	44
Fig. 4.1 FE model for heat conduction analysis	46
Fig. 4.2 Tool work piece geometry for TAFSW experiment	50

Fig. 4.3 Weld cross-section of dissimilar welded joint by TAFSW.....	50
Fig 4.4 Bead surface and cross section of dissimilar butt joint by TAFSW	52
Fig 4.5 Microstructure images of TAFSW dissimilar butt joint	52
Fig. 4.6 Location of thermocouples and corresponding variation of transient temperature in TAFSW (for optimum welding condition)	53
Fig. 4.7 IR camera image showing surface temperature during TAFSW.....	54
Fig. 4.8 Variation of transient temperature in Al-SS400 dissimilar butt joint (for optimum welding condition)	54
Fig 4.9 Experimental measurement of residual stress and locations of strain gauges (in mm) away from weld center line	55
Fig. 5.1 Temperature contour along weld length and thickness obtained at 2sec for Al6061-STS304 butt joint	59
Fig. 5.2 Distribution of temperature at 2 seconds along transverse direction in Al6061-STS304 butt joint	60
Fig 5.3 Time-Temperature plot for Al 6061-STS304 dissimilar joint by TAFSW	61
Fig. 5.4 Temperature contour along weld length and thickness obtained at 2sec for Al6061-SS400 butt joint	63
Fig 5.5 Time-Temperature plot for Al 6061-SS400 dissimilar joint by TAFSW	64

Fig 5.6 Location and time of TIG torch during and after welding	65
Fig 5.7 Temperature contour for TIG preheating obtained at 1sec.....	66
Fig 5.8 Temperature contour for TIG preheating during and after 20mm traverse	67
Fig. 5.9 Temperature contour along obtained at 2sec for Al6061-STS304 butt joint by conventional FSW	67
Fig. 5.10 Temperature contour obtained at 2sec for Al6061-SS400 butt joint by conventional FSW	68
Fig 5.11 Longitudinal stress distribution at 0.2mm below top surface of Al6061-STS 304 dissimilar joint	72
Fig 5.12 Longitudinal stress distribution at 1.4mm below top surface of Al6061-STS 304 dissimilar joint	73
Fig 5.13 Transverse stress distribution at 0.2mm below top surface of Al6061-STS 304 dissimilar joint	73
Fig 5.14 Transverse stress distribution at 1.4mm below top surface of Al6061-STS 304 dissimilar joint	74
Fig 5.15 Longitudinal stress distribution at 0.2mm below top surface of Al6061-SS400 dissimilar joint	76
Fig 5.16 Longitudinal stress distribution at 1.4mm below top surface of Al6061-SS400 dissimilar joint	76

Fig 5.17 Transverse stress distribution at 0.2mm below top surface of Al6061-SS400 dissimilar joint	77
Fig 5.18 Transverse stress distribution at 1.4mm below top surface of Al6061-SS400 dissimilar joint	77
Fig. 5.19 Comparison of numerically simulated and measured temperature history	80
Fig. 5.20 Comparison of experimentally measured and numerically simulated values of longitudinal residual stress (σ_z) at top surface of Al6061-STS304 welded specimen	81

초 록

TIG-FSW 하이브리드 용접을 이용한 이종접합부의 열기계적 거동에 대한 수학적 모델 개발

엠. 에스. 비조이

지도교수: 방 한 서

선박해양공학과

조선대학교 대학원

알루미늄과 스틸의 이종재 FSW 접합 시 장비의 진동 및 톨의 높은 가압력에 의한 톨 마모와 같은 결함이 발생하며, 이러한 결점은 FSW 공정 중 강성이 좋은 재료부분의 예열을 통하여 해결할 수 있다. 소재에 대한 예열을 통하여 가소성이 일어나 일반적인 FSW 의 용접공정과 비슷한 효과를 얻을 수 있다. 본 연구의 TIG 열원은 강성이 높은 재료(STS 304/SS400)의 예열에 이용되므로 알루미늄 합금과 용접 시 건전한 용접부를 얻을 수 있다. TAFSW 를 이용한 이종재료의 3 차원 열전도 해석은 열전달과 온도 분포를 확인하기 위해 실시 되었으며, 이러한 해석결과는 용접부의 잔류응력, 결정립크기 그리고 용접강도를 예측하는데 큰 영향을 미칠 것으로 판단된다.

따라서 이러한 열전도 해석은 스테인리스와 알루미늄합금 이종재료의 맞대기 TAFSW에서 열전달과 온도 분포를 명확하게 확인할 수 있으며, 해석 결과를 이용하여 용접 중 톨 표면에 발생하는 열을 예측하기 위해 3D 모델을

개발하였다. 이종재료 접합 시 발생하는 열에 따른 온도 분포를 분석하기 위하여 기존에 개발된 자체 프로그램을 이용하여 해석하였다.

온도하중은 body force를 적용 하였고, 이에 따른 잔류응력의 특성을 개발된 프로그램을 이용하여 확인하였다. 톨 표면과 시험편에서 발생하는 마찰열과 이동열원을 고려한 입열을 계산하였으며, TAFSW를 이용한 이종재 접합시 발생하는 최고 온도에 대한 예측을 성공적으로 분석하였다.

TIG을 이용한 스테인리스의 예열의 경우 가소성을 형성하여 알루미늄 합금과의 접합을 수월하게 만들어준다. 용접이 진행되는 동안 가장 높은 온도는 고상 마찰부분의 솔더부 아래에서 관찰되었으며, 접합에 따른 금속재 유동은 이종재의 특성상 재료의 물성이 다르기 때문에 스테인레스 스틸부에서 제한됨을 확인할 수 있었다.

FSW 접합 공정에서 예열은 FSW 톨의 마찰면적과 토크를 감소시키는 장점이 있다. 이종접합 공정에서 TAFSW의 경우 접합된 이종재는 잔류 응력 분포가 용접 축에 대하여 비대칭 하였다. 이는 M 형상의 응력분포라 할 수 없으며, 이는 종 방향 잔류응력 최대값이 톨 솔더부의 가장부에서 확인되었기 때문이다.

TAFSW를 이용한 Al6061-ST304/SS400의 이종재 접합의 경우 종방향 응력의 최고값은 알루미늄부가 스틸부 대비 낮게 측정되었는데, 이는 톨의 주된 교반이 알루미늄 부분에서 일어나며 접합을 하는 동안에 알루미늄 합금의 유동은 스틸 방향이고, 강성이 높은 스틸의 영향으로 알루미늄의 소성유동이 방해 받기 때문이다.

또한, 시뮬레이션결과 와 실 측정 온도분포의 결과 비교는 개발하고 사용된 열 전도 모델의 신뢰성을 확인할 수 있었으며, 용접부의 변형 및 잔류응력 매커니즘 형성과 같은 다양한 시뮬레이션에 대한 적용 가능성을 보여주는 결과라 할 수 있다. 개발된 수치해석 모델을 이용한 다양한 이종재료 접합의 온도 및 잔류응력을 예측 할 수 있고, 대부분 알루미늄과 스틸 접합 공정에 적용 될 수 있다. 따라서 본 연구를 실시하여 중공업 분야에서의 TIG를 보조열원으로 한 FSW 의 적용 가능성에 대해 확인하고자 하였다.

또한, 시뮬레이션결과 와 실 측정 온도분포의 결과 비교는 개발하고 사용된 열 전도 모델의 신뢰성을 확인할 수 있었으며, 용접부의 변형 및 잔류응력 매커니즘 형성과 같은 다양한 시뮬레이션에 대한 적용 가능성을 보여주는 결과라 할 수 있다. 개발된 수치해석 모델을 이용한 다양한 이종재료 접합의 온도 및 잔류응력을 예측 할 수 있고, 대부분 알루미늄과 스틸 접합 공정에 적용 될 수 있다. 따라서 본 연구를 실시하여 중공업 분야에서의 TIG를 보조열원으로 한 FSW 의 적용 가능성에 대해 확인하고자 하였다.

Chapter 1

INTRODUCTION

Advance joining technologies allow manufactures to use the latest materials and designs to enhance their products performance, reduce manufacturing costs and decrease life cycle costs. The joining needs of each industry vary depending upon its products and the pressures for most cost effective productivity. Heavy industries, especially shipyard, aerospace, petroleum/energy and automotive rely heavily on welding.

In recent years, the use of aluminium in manufacturing has become more prevalent because of its light weight and other attributes that make it an attractive alternative to steel. Aluminium in its pure form suffers from poor strength, but when alloyed with other metals the unique combination is an attractive element with wide range of attractive properties. Aluminium has several chemical and physical properties that need to be understood when using the various joining processes. The most common method of welding aluminium is tungsten inert gas (TIG), but this method is much more expensive than ordinary gas welding and a defect free weld is impossible. A further challenge is to weld dissimilar aluminium alloys and next, to join aluminium alloys to steels by fusion welding process. However, the stability and integrity of the welded joints between dissimilar materials is frequently problematic, and depending on the particular materials and configurations, welding of dissimilar materials has also proven to be difficult under field conditions. Thus, dissimilar material arc fusion welds are often considered to have an increased risk of failure. The demand of multi material

constructions, especially the combination of steel with aluminium to reduce total weight of the component is increasing day by day.

Friction stir welding (FSW) patented by W.M. Thomas and his colleagues of The Welding Institute (TWI), UK, in 1991 is an innovative joining process which can weld dissimilar alloys traditionally considered unweldable. This emerging solid state welding process shows great promise to improve the quality of welds in high strength aluminium alloys with considerable weight savings in lightweight construction, when compared with conventional welding techniques and keeping the thermo-mechanical stresses and deformations of traditional welding methods to a minimum. Additionally, the process does not use fillers and, like fusion welding, eliminates the need for fasteners, which add weight to a structure. The lack of knowledge about the analytical and numerical approaches to TIG assisted FSW (TAFSW) parameters and their interaction is the motivation behind this study. Welding simulation capabilities and integration with system models of TAFSW can compress the time needed between the design phase and production start-up. The capability to simulate thermal and mechanical changes caused by welding and to predict residual stress will help product development teams select the best welding option and better predict weld life time and performance. Benefits include reduced production costs, reduced reworking requirements and otherwise improved weld quality, lower energy consumption and market growth.

1.1 Research Background

Dissimilar material joints are used in structures where high strength and light weight are desirable. The growing trend for light weight structural designs, especially in automotive, aerospace and ship building has made aluminium alloys to be used as an

alternative material [1]. Dissimilar materials joining which has been widely used in aerospace and automotive can provide opportunities in construction and other heavy industries. Breakthroughs in the technology for joining dissimilar materials could lead to new manufacturing strategies that could reduce costs, improve productivity, and open up new markets for welded structures and components. With this, new trend of joining aluminium to steels with required improvements in weld quality has made newer challenges to the manufactures. Friction stir welding (FSW) offers many potential benefits such as low distortion, improved joint efficiency (tensile strength), improved process robustness, etc., for welding aluminium alloys [2][3].

Various research works has already been reported about the application of FSW process on dissimilar material joining [4-9]. However when joining aluminium to steel, equipment rigidity, high force to move the tool and high tool wear rate during FSW induces weld defects. These drawbacks can be overcome by localised preheating the surface of harder material ahead of the rotating tool pin during FSW process. A volume of the material plasticizes during preheating and further to this the welding process can be carried out in the same way as conventional FSW. Kong et al. [10] has demonstrated the use of laser for preheating the workpiece surface ahead of the FSW process. However, only a narrow portion of the workpiece can be preheated by using laser when compared with TIG arc which allows the preheating over wider area. Also, preheating by TIG arc offers several advantages such as good control over current, absence of spatter, high efficiency and low cost compared to laser.

Despite the in-depth research over the past decade, the fundamentals of the FSW process are not well understood for dissimilar butt joints. Though many experimental and analytical research works are going on to describe the FSW process, no report has been seen in the open literature on TAFSW of dissimilar materials.

Therefore, as an access to knowledge and practical information, it is necessary to obtain a closed form solution for thermo-mechanical behavior of dissimilar joint during TAFSW from analytical and numerical modeling (3D). Hence this work intends to investigate the feasibility of joining aluminium alloy 6061-T6 (Al6061) with Stainless steel 304 (STS304) using TIG assisted solid state joining process where melting of materials is not an inherent demand of the principle and technology of the process. Three dimensional Finite element simulation has been employed to predict the heat distribution and residual stress characteristics of the dissimilar specimen during TAFSW. For this, an analytical model to determine the heat generation during FSW process has been developed and described in chapter. The model presented use relatively simple process model equations and reliably predicts the heat distribution and residual stresses which can be applied for variety of FSW process environments. The accuracy of the finite element model is evaluated based on experimental results and the results of analytical solution.

1.1.1 Research methodology

The methodology of research is given in Fig.1.1:

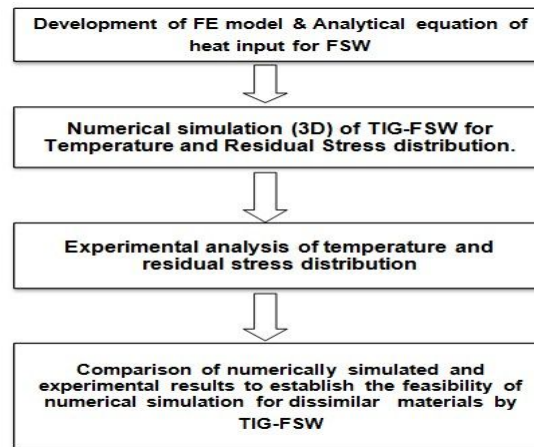


Fig.1.1 Outline of Research methodology

1.2 Literature review

1.2.1 Friction Stir welding

In friction stir welding a rotating pin emerging from a cylindrical shoulder is plunged between two pieces of sheet and moved forward along the joint line. The mechanical interaction, due to the velocity difference between the rotating tool and the stationary work piece, produces heat by frictional work and material deformation. This heat dissipates into the surrounding material, the temperature rises and the material softens. After these two operations the actual welding process can be initiated by moving either the tool or the work piece relative to each other, along the joint line leaving a solid phase bond between the two pieces to be joined [11]. The schematic of FSW is shown in Fig.1.2.

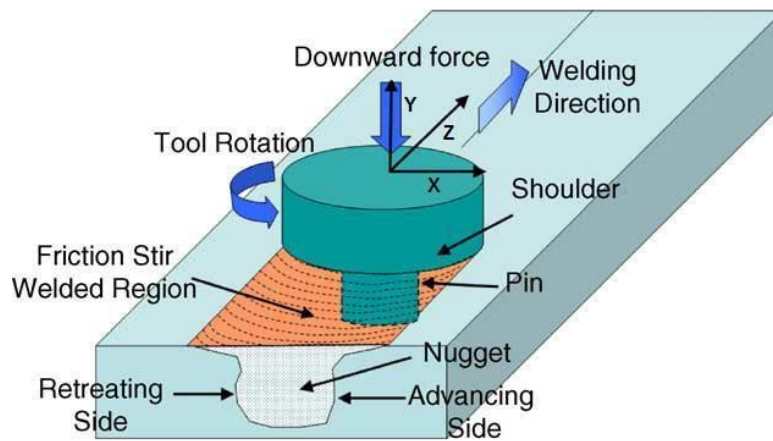


Fig 1.2 Schematic of friction stir welding process

This innovative technology confers an extra-strong welded joint, as well as numerous other advantages. Because the highest temperature in the FSW process is lower than the melting temperature of the work piece material, FSW yields fine

microstructures, absence of cracking, low residual distortion and no loss of alloying elements, which are the main advantages of the process. Nevertheless, the process will form a softened heat affected zone and a residual stress region, parallel to the welding line. The friction stir welding equipment is completely automatic and easy to use. It requires a minimal amount of surface preparation, hence saves operating time, and the absence of pores makes for a stronger weld.

1.2.2 Phases of FSW process

Plunging: The rotating welding tool is plunged vertically into the joint line between the weld pieces.

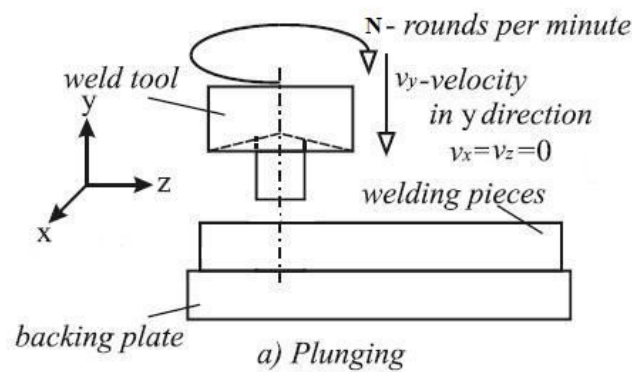


Fig 1.3 Plunging phase of FSW tool to work piece

Dwelling: The tool stays steady relative to the work pieces but still constantly rotating. The mechanical interaction, due to the velocity difference between the rotating tool and the stationary work piece, produces heat by frictional work and material deformation. This heat dissipates into the surrounding material, the temperature rises and the material softens.

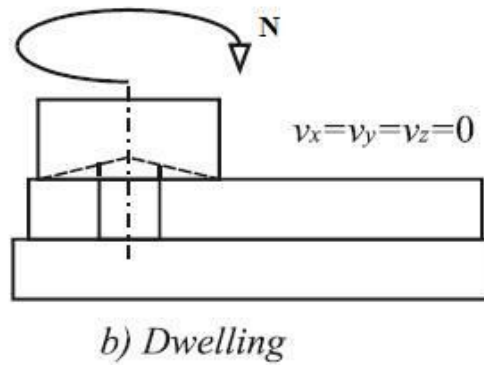


Fig 1.4 Dwelling phase of FSW tool to work piece

Welding: The actual welding process can be initiated by moving either the tool or the work piece relative to each other, along the joint line.

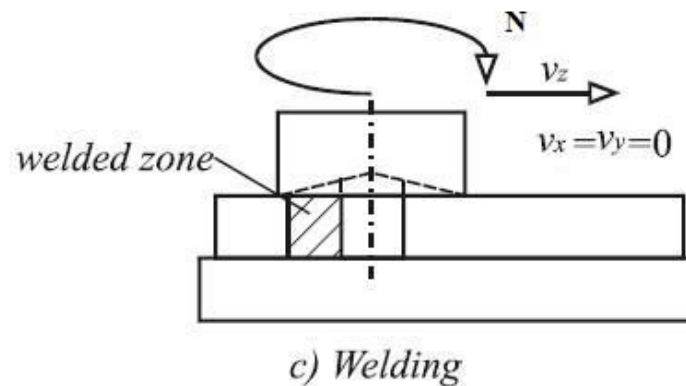


Fig 1.5 Welding phase of FSW

Pulling out: After welding phase, traversal movement between tool and weld pieces stops but welding tool continues its rotation. When the weld distance is covered, the tool is pulled out of the work piece leaving behind an exit hole as a footprint of the tool.

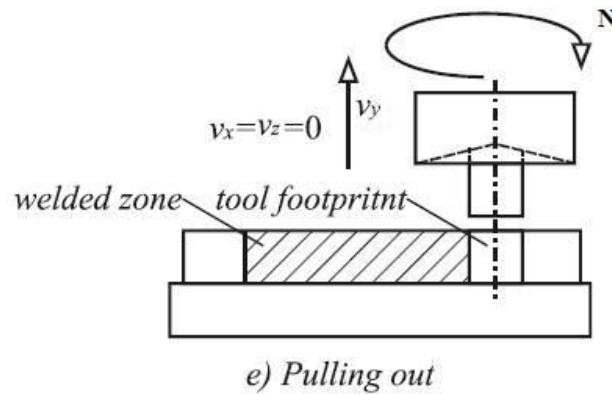


Fig 1.6 Pulling out of FSW tool from work piece

1.2.3 TIG assisted FSW process

During FSW the forces on the tool and maximum welding speed are affected by the temperature distribution in the material in front of the tool. Higher temperatures can be obtained by increasing the rotational speed of the tool. However, there appears to be a limit to this method of heat input. The research currently undertaken is directed towards using an auxiliary heat source in front of the tool to preheat harder material. A literature review was conducted, and initial trials indicate the friction stir process can readily weld Stainless steel plate. TIG-assisted friction stir welding (TAFSW) that is developed in our welding laboratory at Department of Naval Architecture and Ocean engineering, Chosun University, is a solid-state welding process that integrates TIG preheating into friction stir welding. TIG-FSW introduces additional local heating on the surface of the harder material, without melting of the material, immediately ahead of the weld zone so that less mechanical energy delivered through the tool must be converted into heat. This reduces the tool forces, deflections in the machine and fixture, and may enable higher weld speeds. Pre-heating and softening the harder base metal with an arc prior to welding can significantly reduce tool wear during friction stir

welding of hard materials such as steels, titanium alloys and metal-matrix composite. TIG arc pre-heating prior to FSW can also join materials with very different physical properties, such as aluminium and copper, or aluminium and steel, something that is difficult to do with conventional FSW. Fig 1.7 shows the schematic of TIG –FSW process.

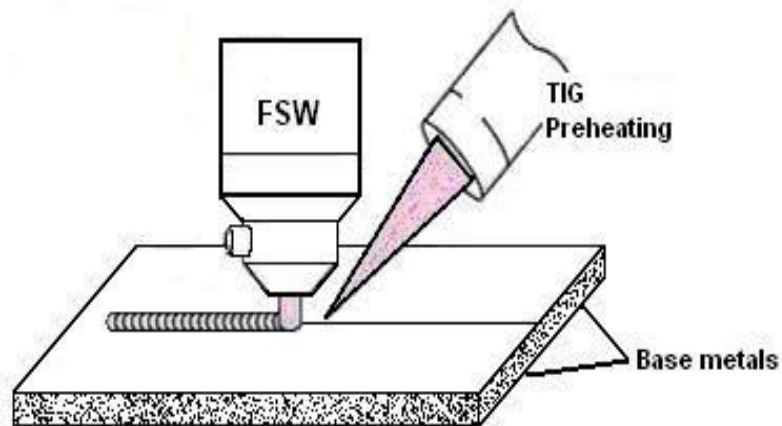


Fig 1.7 Schematic of TIG assisted friction stir welding

1.2.4 Characteristics of Base materials

Furthermore, the steel materials welded to aluminum alloys that join technical parts are in great demand. For example, a vehicle's main structure, such as the steel-made chassis module, can be joined with secondary structural elements of aluminum alloy materials. Aquatic transportation vehicles prefer hulls made of steel and aluminum alloys; the under-water surface is made of steel, whereas, above the water surface, it is possible to use aluminum alloy. This structure not only lowers the center of gravity of the vehicles, but also achieves the reduction of their weight. [12].

a) Aluminum 6061-T6

The unique combination of light weight and relatively high strength makes Aluminium the second most popular metal that is welded. Al 6061 is one of the most widely used alloys in the 6000 series. Al 6061 is a precipitation hardening aluminum alloy, containing magnesium and silicon as its major alloying elements. This standard structural alloy, one of the most versatile of the heat treatable alloys, is popular for medium to high strength requirements and has good toughness and excellent welding characteristics. Al 6061 has excellent corrosion resistance to atmospheric conditions and good corrosion resistance to sea water. The chemical composition and mechanical properties of Al 6061-T6 are given in Table. 1.1.

Table 1.1 Chemical composition and mechanical properties of Al 6061-T6

Material	Chemical composition (wt%)								
Al6061 -T6	Al	Fe	Si	Cr	Mg	Ti	Cu	Mn	Zn
	98	0.7	0.4-0.8	0.04-0.35	0.1	0.03	0.15-0.4	0.15	0.25
	Mechanical properties								
	Yield stress (MPa)		Elongation (%)		Tensile stress (MPa)		Heat conduction coff.		Melting Point
	276		12		310		0.4		650

b) Stainless Steel (STS 304)

Grade 304 is the standard "18/8" stainless; it is the most versatile and most widely used stainless steel, available in a wider range of products, forms and finishes than any other. It has excellent forming and welding characteristics. It is widely used in components for applications in the industrial, architectural, and transportation fields. Grade 304 with its higher carbon content finds application at elevated temperatures. The austenitic structure also gives these grades excellent toughness, even down to

cryogenic temperatures. AISI 304 Stainless Steel is of marine grade and can withstand extended exposure to salt water in extreme conditions. The chemical composition and mechanical properties of STS304 are given in Table. 1.2.

Table 1.2 Chemical composition and mechanical properties of STS304

Material	Chemical composition (wt%)								
STS 304	C	Si	Mn	P	S	Ni	Cr	Mo	
	0.08	1.00	2.00	0.040	0.030	8.0~10.50	18.0~20.0	-	-
	Mechanical properties								
	Yield stress (MPa)		Elongation (%)		Tensile stress (MPa)		Heat conduction coeff.		Melting Point
	265		55		628		0.039		1450

c) SS400 steel

SS400 steel plate is one mainly of Carbon and low alloy steel. SS400 steel plate would be used to build containers which can bear low temperature sea water. It is also applied in construction of bridge, ship, automobile and other structures. The chemical composition and mechanical properties of SS400 are given in Table. 1.1.

Table 1.3 Chemical composition and mechanical properties of SS400

Material	Chemical composition (wt %)						
SS 400	C	Si	Mn	P	S	Al	N
	0.12	0.18	1.0	0.0015	0.060	0.038	0.006
	Mechanical properties						
	Yield Stress (MPa)		Elongation (%)		Tensile stress (MPa)		Density (g/cc)
	235		19		400 ~ 510		7.86

1.2.5 Temperature dependent material properties of base materials

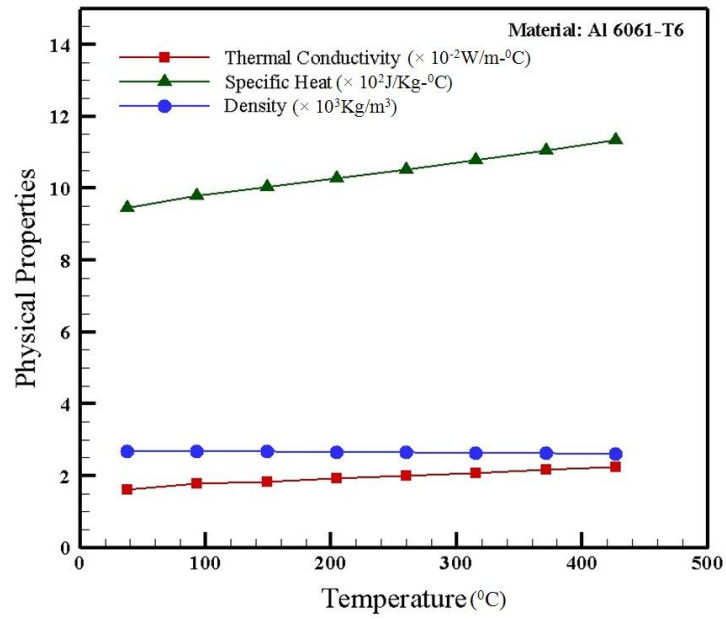


Fig.1.8 Physical properties of Al-6061-T6

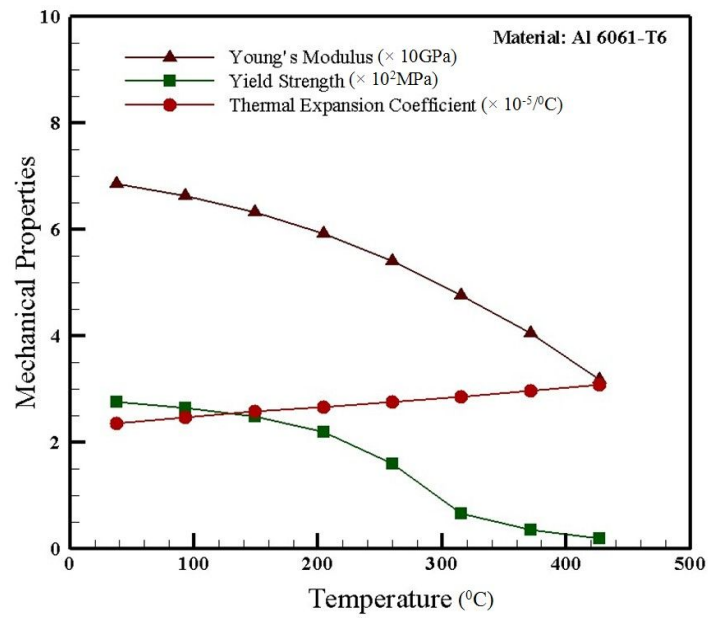


Fig.1.9 Mechanical properties of Al-6061-T6

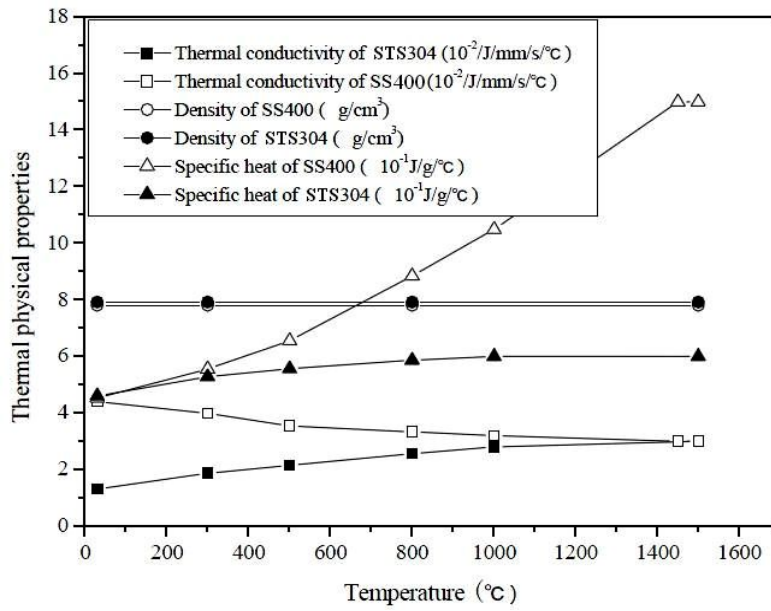


Fig.1.10 Physical properties of STS304 and SS400

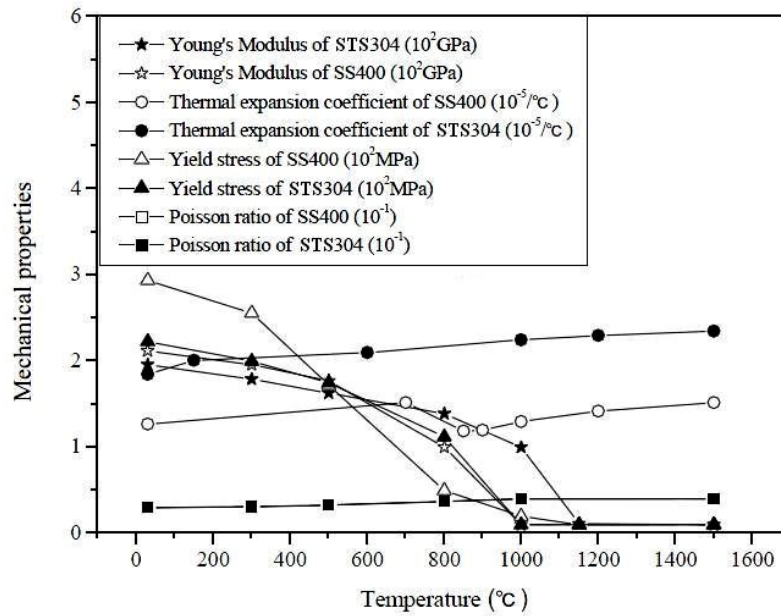


Fig.1.11 Mechanical properties of STS304 and SS400

1.2.6 Thermal Modeling of Friction Stir Welding

Understanding the heat generation and the temperature history during the FSW process is the first step towards understanding the thermo-mechanical interaction taking place during the welding process. The initial modeling approaches focused on approximate estimation of heat generated during the FSW process. Gould and Feng [12] developed a preliminary thermal model to predict the temperatures of friction stir welds using the Rosenthal equations to describe a moving heat source. The heat input was described as a function of process parameters such as tool rpm and force on tool.

In order to study the heat transfer in friction stir welding, Chao, Qi and Tang [13] formulated a boundary value problem for tool and workpiece. They determined the frictional heat flux from the measured transient temperature fields obtained in the finite element analyses. The flow of material around the tool is predicted by Colegrove *et al.* [14] using a finite element based thermal model of FSW including backing plate. In their work, the heat input was fitted through iterative process for verification between the modeled and experimental values.

An input torque based thermal model for prediction of temperature in friction stir welds of Al-6061-T6 alloy was developed by Khandkar *et al* [15]. In their model, the heat generated by tool rotation and linear traverse of shoulder and pin, has been correlated with actual machine power input which was applied as a moving heat to obtain the temperature distribution across the weld.

Song and Kovacevic [16] proposed a coupled heat transfer model of both the tool and the workpiece for FSW to include the tool penetration and pulling out phase. A moving coordinate was adopted to reduce the difficulty of modeling the heat generation due to the movement of the tool pin. The finite difference method was used for solving

the control equations and the results obtained were in good agreement with the experimental results.

Vilaca *et al.* [17] developed an analytical thermal model which included simulation of the asymmetric heat field under the tool shoulder resulting from viscous and interfacial friction dissipation. The analytical model also considered the influence of hot and cold FSW conditions into the heat flow around the tool.

The focus of all the thermal models was to understand the process of heat generation and to predict the temperature distribution in the workpiece and tool. A thermal model forms the basis for the development of mechanical and microstructural models.

Thermomechanical models for FSW were developed and studied in order to estimate residual stress and distortions in workpiece resulting from welding process. One of the first thermomechanical models for FSW was studied by Chao and Qi [18] in which decoupled heat transfer and a subsequent thermomechanical analysis for Al 6061-T6 was used. Heat generated from friction between tool shoulder and workpiece was implemented as the heat input. The empirical equation for calculating the heat input to the workpiece is given by equation (1.1).

$$q(r) = \frac{3Qr}{2\pi(r_0^3 - r_i^3)} \quad \text{for } r_i \leq r \leq r_0 \quad (1.1)$$

where $q(r)$ is the rate of heat input, r_o and r_i are the radii of the shoulder and the tool

pin, and Q is the total rate of heat input to the workpiece expressed as shown in

equation(1.2).

$$Q = \frac{\pi \omega \mu F (r_o^2 + r_o r_i + r_i^2)}{45(r_o + r_i)} \quad (1.2)$$

where, ω is the tool rotational speed, μ is the frictional coefficient, and F is the

downward force. The total heat input and heat transfer coefficient were estimated by fitting the measured temperature data with the analytical model by a trial and error approach. The temperatures thus obtained from the analysis were used to determine the residual stress retained in the friction stir welds.

Chen and Kovacevic [19] proposed a 3D FEM model to study the thermal history and thermomechanical process in butt welding of aluminium alloy 6061-T6. In his model the mechanical reaction of the tool and thermomechanical processes of the

welded material was incorporated. The friction between the material, the pin and the shoulder was included in the heat source. The residual stress developed in the plate was measured using X-ray diffraction technique and the measured results were used to validate the efficiency of the proposed model. From the study, it was reported that fixturing release to the welded plates affected the stress distribution of the weld.

Zhu and Chao [20] used FEM code WELDSIM to conduct the nonlinear thermal and thermomechanical simulations on 304L stainless steel friction stir welded plates. Initially, a heat transfer problem was formulated as a standard boundary value problem and was solved using the inverse analysis approach. The total heat input and heat transfer coefficient were estimated by fitting the measured temperature data with the analytical model. Later, the transient temperature outputs from the first stage were used to determine residual stresses in the welded plates using a three-dimensional elastic plastic thermomechanical model. Convection and radiation were assumed to be responsible for heat loss to the ambient on the surface. Their model provided good match between experimental and predicted results. They reported that the residual stress in the welds after fixture release decreased significantly as compared to those before fixture release.

Soundararajan *et al.* [21] predicted the stress at workpiece and backing plate interface using a FE thermomechanical model with mechanical tool loading considering a uniform value for contact conductance. Khandkar *et al.* [22] developed coupled finite element models to predict residual stress in AA-2024, AA-6061 and SS 304L friction stir welds. In their models, the temperature history predicted by the thermal model was sequentially coupled to a mechanical model to assess the residual thermal stresses developed during the welding. It was found that clamping constraints and their

locations had significant localized effects on the stress components in the unaffected base metal beyond the heat-affected zone.

Nandan et al. [24] solved the equations of conservation of mass, momentum, and energy in three dimensions using spatially variable thermo physical properties and non-Newtonian viscosity. In general, all the multi-phase materials, in which the material properties are varied gradually in a predetermined manner, fall into the category of functionally gradient materials. Li et al. [25] proposed the FGM concept to determine thermal stresses using 3D model of Al 6061 and 304L dissimilar joint by FSW.

This study intends to gain a clear physical insight in to the thermal and residual stress characteristics in dissimilar butt joint of aluminium alloy (Al 6061-T6) and stainless steel 304 (STS 304) during TAFSW.

Schmidt et al. [25] sought to establish an analytical model for heat generation during friction stir welding based on different assumptions of the contact condition between the rotating tool surface and the weld piece. The material flow and heat generation are characterized by the contact conditions at the interface and are described as sliding, sticking or partial sliding/sticking. Different mechanisms of heat generation were found to be behind each contact condition. The analytical expression for the heat generation in this work is a modification of previous analytical models known from the works by Colligan and Colegrove [26] [27]. In these works, both conical surfaces and different contact conditions were considered. Colegrove estimated the fraction of heat generated by probe is to be as high as 20%, which leads to the conclusion that the analytical estimated probe heat generation contribution is not negligible.

The current investigation utilizes Schmidt et al. [25] frictional model for heat generation to determine the heat input. Schmidt et al. provide a comprehensive

discussion on the calculation of interfacial heat generation rates during FSW which includes heat generation contributions from specific tool surfaces. A contact state variable has been defined to describe the condition at the contact interface and is introduced in the expression for the analytical heat generation to accommodate sliding/sticking contact condition and the final expression for the heat generation demonstrates flexibility for applying to a dissimilar butt joint model. Finite element analysis of dissimilar joint for particular tool geometry and material properties is conducted based on steady state heat transfer model developed by Rajesh et al. [28]. For numerical simulation of steady state 3D heat transfer analysis of TAFSW, in-house developed computer program to simulate heat transfer is used with adequate modifications [29]. Initially, thermal analysis for dissimilar butt joint by TAFSW was conducted using temperature dependent thermal material properties [30]. The computed temperature history in each node from the thermal analysis is input as the thermal load in the residual stress analysis.

Chapter 2

ANALYTICAL MODEL FOR DISSIMILAR JOINT

BY TAFSW

2.1 Introduction

The current investigation utilizes Schmidt [25] FSW model in order to estimate the heat generation based on assumptions for different contact conditions at the tool/matrix interface in FSW joints. Using the analytical model in comparison with the experimental result estimates the maximum temperature at tool-work piece interface during TAFSW and residual stresses during welding. The analytical model for heat generation by friction stir welding (FSW), as proposed by H.Schmidt and J.Hattel [25] [32] [33], is based on the different assumptions of contact condition between the rotating tool surface and the weld piece. The material flow and heat generation are characterized by the contact conditions at the interface, and are described as sliding, sticking or partial sliding/sticking. Different mechanisms of heat generation are behind each contact condition. This research work is focused on joining of dissimilar materials by FSW using TIG preheating. In that case it is assumed that welding is done with combination of the sliding and sticking in the contact of the tool and work pieces. The quantity of heat input from the TIG arc is added to the heat input from FSW process based on super position principle.

2.2 Tool geometry

In FSW process, after an initial transient period, the torque does not change during welding which reflects a steady state welding condition. In general, two tool surfaces are needed to perform the heating and joining processes in the friction stir weld: the shoulder and the probe. Shoulder is massive cylindrical part that carries smaller cylindrical part – probe as shown in Fig 2.1. There are three surfaces of the tool that perform the heat generation by friction and enable joining of weld pieces. Probe has two surfaces that can generate heat – the tip and the side of the probe. Shoulder surface is the area where the majority of the heat is generated, whereas the probe

surface is where the work pieces are joined together and only a fraction of the total heat is generated. Second, the shoulder confines the underlying material so void formation and porosity behind the probe is prevented. The conical tool shoulder helps establish a pressure under the shoulder, but also acts as an escape volume for the material displaced by the probe during the plunge action. The probe height is limited by the work piece thickness; the probe tip must not penetrate the work piece, or damage the backing plate or support frame is unavoidable.

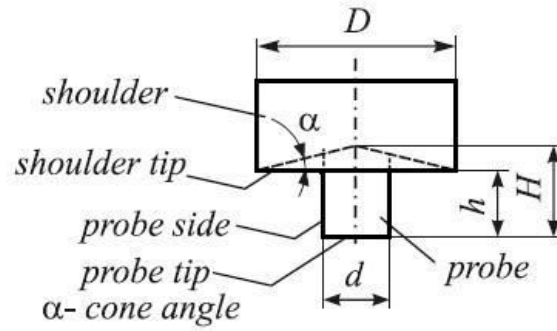


Fig 2.1 Basic shape of the FSW tool assumed for analytical calculation [25]

2.3 Contact condition

The contact condition is the most critical part of the numerical model when modeling the FSW process. The TIG-FSW and LFSW follows the same principles of modeling heat generation of FSW followed by H.Schmidt and J.Hattel, but only difference is that the preheating by TIG is considered here. The shear forces between the tool surface and the matrix is described by Coulomb law of friction. This estimates the critical friction stress necessary for contact condition and predicts the mutual motion between the two segments-whether they stick or slide and is given as:

$$\tau_{friction} = \mu p \quad (2.1)$$

$\mu \rightarrow$ Friction coefficient

$p \rightarrow$

Uniform pressure at contact interface (Pa)

The normal interpretation of Coulomb's law is based on rigid contact pairs, without respect to the internal stress. To describe more specific interpretation of Coulomb's law for FSW, three contact conditions is defined.

Sticking condition: The matrix surface will stick to the moving tool surface segment, if the friction shear stress exceeds the yield shear stress of the underlying matrix. In this case, the matrix segment will accelerate along the tool surface (finally receiving the tool velocity), until equilibrium state is established between the contact shear stress and the internal matrix shear stress. At this point, the stationary full sticking condition is fulfilled. In conventional Coulomb's friction law terms, the static friction coefficient relates the reactive stresses between the surfaces.

Sliding condition: If the contact shear-stress is smaller than the internal matrix yield shear stress, the matrix segment volume shears slightly to a stationary elastic deformation, where the shear stress equals the 'dynamic' contact shear stress. This state is referred to as the sliding condition.

Partial sliding/sticking: This a mixed state condition between the sticking and sliding. In this case, the matrix segment accelerates to a velocity (v_{matrix}) less than the tool surface velocity (v_{tool}), where it stabilizes. The equilibrium establishes when the 'dynamic' contact shear stress equals the internal yield shear stress due to a quasi-stationary plastic deformation rate. This is referred to as the partial sliding/sticking condition. In this model, there is no difference between the dynamic and the static friction coefficients.

Hence a contact state variable, δ , is defined which relates the velocity of the contact points at the matrix surface relative to the tool point in contact. This parameter is a dimensionless slip rate defined as

$$\delta = \frac{v_{matrix}}{v_{tool}} = 1 - \frac{\dot{\gamma}}{\dot{\gamma}_0} \quad - 22 -$$

$$(2.2)$$

$$\text{Where slip rate, } \dot{\gamma} = v_{tool} - v_{matrix} \quad (2.3)$$

Table 1 gives the Definition of contact condition, velocity/shear relationship and state variable (dimensionless slip rate).

Table 2.1: Definition of contact condition related to tool and matrix velocity [25]

Condition	Matrix velocity (m/sec)	Tool velocity (m/sec)	Shear stress (Pa)	State variable
Sticking	$v_{matrix} = v_{tool}$	$v_{tool} = \omega r$	$\tau_{friction} > \tau_{yield}$	$\delta = 1$
Sticking / sliding	$v_{matrix} < v_{tool}$	$v_{tool} = \omega r$	$\tau_{friction} \geq \tau_{yield}$	$0 < \delta < 1$
Sliding	$v_{matrix} = 0$	$v_{tool} = \omega r$	$\tau_{friction} < \tau_{yield}$	$\delta = 0$

2.4 Analytical estimation of heat generation

For TIG-FSW the partial sliding/sticking condition is assumed based on a general assumption of uniform contact shear stress $\tau_{contact}$ and further distinguished by assuming a specific contact condition. In the case of the sticking condition, the shearing is assumed to occur in a layer very close to the interface and in the sliding condition the shear is assumed to take place at the contact interface.

For the analytical estimation, a simplified tool design with a conical or horizontal shoulder surface, a vertical cylindrical probe side surface and a horizontal (flat) probe tip surface is assumed. The conical shoulder surface is characterized by the cone angle α , which in the case of a flat shoulder, is zero. The simplified tool design is

as given in Fig 2.2, where Q_1 is the heat generated under the tool shoulder, Q_2 at the tool probe side and Q_3 at the tool probe tip, hence the total heat generation, $Q_{\text{total}} = Q_1 + Q_2 + Q_3$. Radius of probe and shoulder is given as R_{probe} and R_{shoulder} respectively.

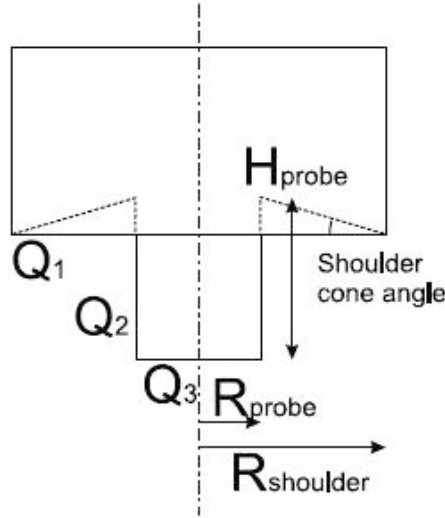


Fig 2.2 Heat generation contributions in analytical estimates [22]

2.4.1 Heat generated at tapered pin surface

Fig.2.3 shows the schematic of FSW tool used in experiment. R_s , R_1 and R_2 are the radius of tool shoulder, pin top and pin bottom respectively. 'H' is the height of the pin. In FSW, the heat energy is generated by friction and deformation process at the interface of the shoulder/workpiece and tool pin/ workpiece [25].

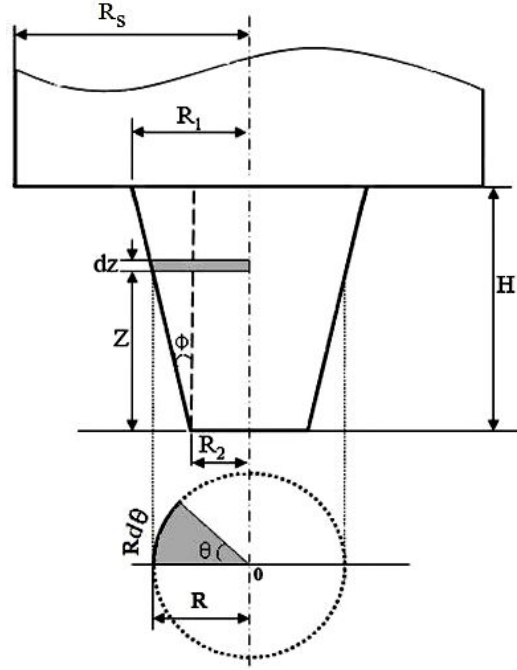


Fig. 2.3 Schematic drawing of tool and infinitesimal segment area at pin surface

The total heat generation is given as

$$Q_{total} = Q_{shoulder} + Q_{pinsurface} + Q_{pinbottom} \quad (2.4)$$

The heat generation from tool shoulder and pin bottom is [32, 33]

$$Q_{shoulder} = \int_0^{2\pi} \int_{R_1}^{R_s} \omega \tau_{contact} r^2 dr d\theta \quad (2.5)$$

$$Q_{shoulder} = \left[\frac{2}{3} \pi (\delta \tau_{yield} + (1 - \delta) \mu p) \times \omega (R_s^3 - R_1^3) \right] \quad (2.6)$$

$$Q_{shoulder} = \int_0^{2\pi} \int_0^{R_2} \omega \tau_{contact} r^2 dr d\theta \quad (2.7)$$

$$Q_{pinbottom} = \left[\frac{2}{3} \pi (\delta \tau_{yield} + (1 - \delta) \mu p) \times \omega \times R_2^3 \right] \quad (2.8)$$

Where, p is the tool pressure, ω is the tool angular rotation speed, μ is the coefficient of friction and δ is the contact slip. The contact shear stress for sticking condition is

$$\tau_{contact} = \tau_{yield} = \frac{\sigma_{yield}}{\sqrt{3}} \quad \text{and shear stress for slipping condition is } \tau_{contact} = \mu p \quad [32].$$

A uniform contact pressure at tool/work piece interface is assumed in this analysis as detailed contact pressure at this region is unknown.

To find the heat generated at the pin surface, consider an element of depth 'dz' with radius 'R' at a height 'z' from the pin bottom surface.

$$\text{From the figure,} \quad \tan \phi = \frac{(R_1 - R_2)}{H} \quad (2.9)$$

$$R = R_2 + z \tan \phi \quad (2.10)$$

$dA = R d\theta dz$, where 'dA' is the infinitesimal segmental area

If ' $\tau_{contact}$ ' is the uniform contact shear stress at 'dA', then the infinitesimal force on

$$\text{segment, } dF = \tau_{contact} dA = \tau_{contact} R d\theta dz \quad (2.11)$$

$$\text{Torque, } dM = R dF = \tau_{contact} R^2 d\theta dz \quad (2.12)$$

Therefore, heat generated from infinitesimal surface segment is,

$$dQ_{pinsurface} = \omega dM = \omega \tau_{contact} R^2 d\theta dz \quad (2.13)$$

$$Q_{pinsurface} = \int_0^{2\pi} \int_0^H \omega \tau_{contact} R^2 d\theta dz \quad (2.14)$$

' $\tau_{contact}$ ' is the uniform contact shear stress at 'dA'.

$$Q_{pinsurface} = \int_0^{2\pi} \int_0^H \omega \tau_{contact} (R_2 + z \tan \phi)^2 d\theta dz \quad (2.15)$$

$$Q_{Pinsurface} = 2\pi \omega \tau_{contact} \left(R_2^2 H + R_2 H^2 \tan \phi + \frac{H^3}{3} \tan^2 \phi \right) \quad (2.16)$$

Hence for heat energy generated from the surface of tapered pin is

$$Q_{pinsurface} = \left[2\pi(\delta\tau_{yield} + (1-\delta)\mu p) \times \omega \times \left(R_2^2 H + R_2 H^2 \tan \phi + \frac{H^3}{3} \tan^2 \phi \right) \right] \quad (2.17)$$

When $\phi = 0$, equation (2.17) gives the heat generation for cylindrical pin surface [25].

2.4.2 Heat input calculation for Preheating TIG Heat source

During preheating, the arc energy acts on the work piece surface as surface heat source and conducts into the work piece. Gaussian distribution is applied to the heat source and the surface heat flux of arc is given by [43]

$$Q_{arc}(x, y, t) = \frac{3\eta V I_m}{\pi r_a^2} \exp\left(-3 \frac{r^2}{r_a^2}\right) \quad (2.18)$$

$$r^2 = (x - w_s t)^2 + y^2 \quad (2.19)$$

η is the arc efficiency, V is the voltage (V), I_m is the mean current (A)[44] and w_s is the welding speed (mm-s^{-1}) r_a is the effective arc radius (mm).

$$\text{Mean current } I_m = \frac{I_p \times T_p + I_b \times T_b}{T_p + T_b} \quad (2.20)$$

I_p pulse current (A)

I_b base current (A)

T_p pulse current duration (ms)

T_b base current duration (ms)

Heat flux for heat input element is calculated by multiplying element volume and uniform heat flux per volume. Uniform heat flux is obtained by dividing total heat input by the product of volume of heat source and heating time per unit welding length.

Chapter 3

HEAT TRANSFER AND RESIDUAL STRESS ANALYSIS

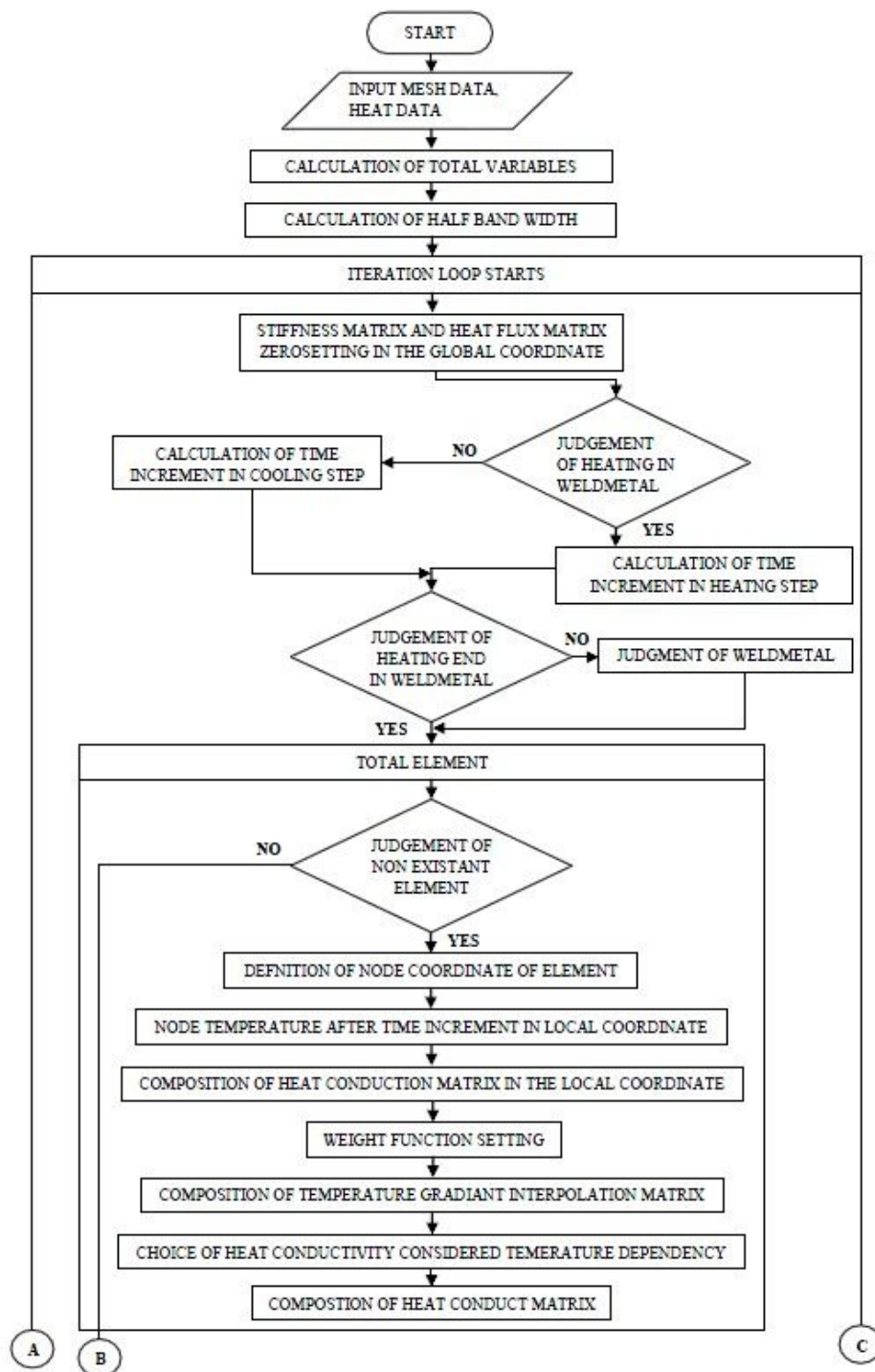
3.1 Introduction

Heat flow during welding of dissimilar metals can strongly affect phase transformations on the base metals and, therefore, the microstructure and properties of the welded joint at the stir zone and heat affected zone where the high temperatures are reached. It is also responsible for weld residual stresses and distortions. For this reason, visualization of the temperatures distribution during TAFSW process is very important to estimate the peak temperatures at tool –work piece interface. Because of different thermo-physical values of the base metals, heat flow might be asymmetrical with respect the welding direction. Residual stresses and plastic strains produced by localised heating and cooling during welding are the major concerns which are detrimental to the structures leading to distortion and even the premature failure to the welded parts. Even if FSW is a welding process operating in the solid phase during joining, the rigid clamping used in FSW impedes the contraction of the weld nugget and heat affected zone (HAZ) during cooling in both longitudinal and transverse directions and gives rise to residual stresses [31]. In dissimilar welded joints, non uniform distribution of temperature field due to different thermal properties of materials exhibits complex welding residual stresses.

The heat flow equations are governed by partial nonlinear differential equations. This means that analytical solutions of the equations may be difficult, and even impossible, to obtain without assumptions, simplifications and loss of generality.

The most important characteristics in welding are the fact that peak temperatures are very high, temperature gradients are high and temperature fluctuates rapidly. This means that in order to capture the speed and complexity of the temperature distribution in a welding specimen, the model needs to have a high order of accuracy. On the other hand, high accuracy often leads to high order of complexity, which may lead to a model difficult to control.

The basis of the finite element technique (to tackle the thermal elastic–plastic problem) is to change the nonlinearity relation of the stress and strain into a linear one during the loading process. The external force does not have any effect on welding, but loading is due to the change in temperature. The flow diagram of the program for heat conduction and residual stress are shown in Fig3.1 and Fig 3.2.



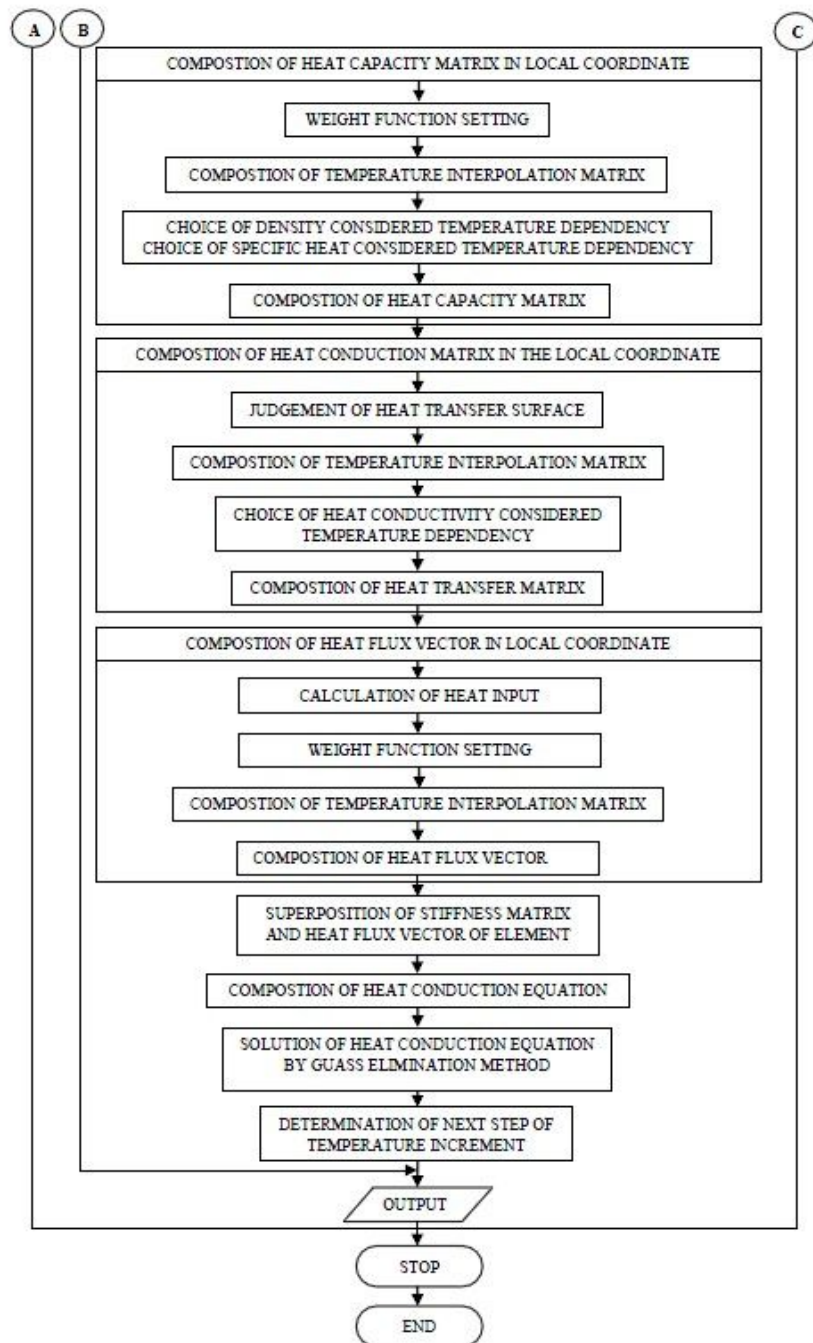
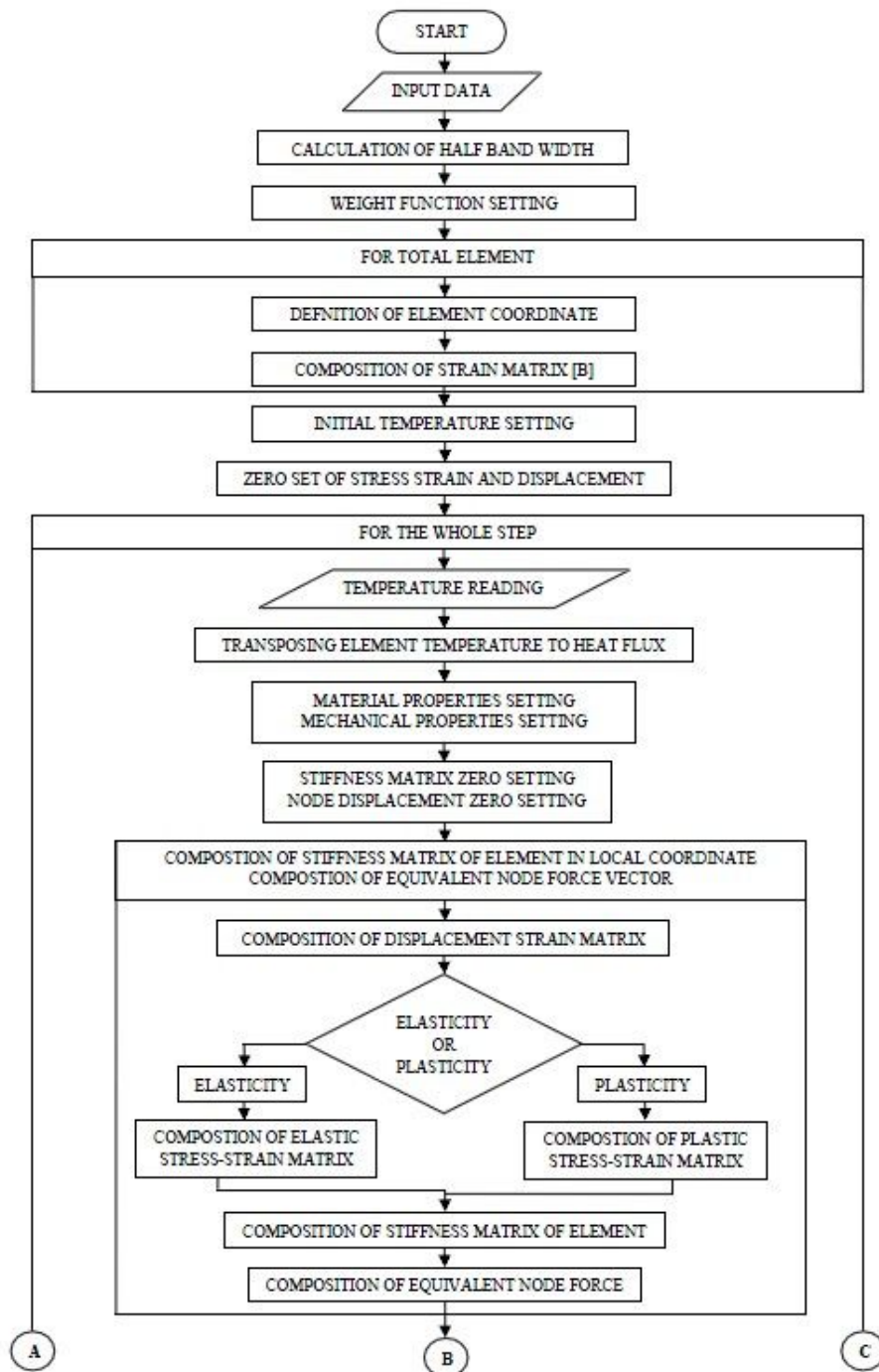


Fig 3.1 Flow diagram for heat conduction program



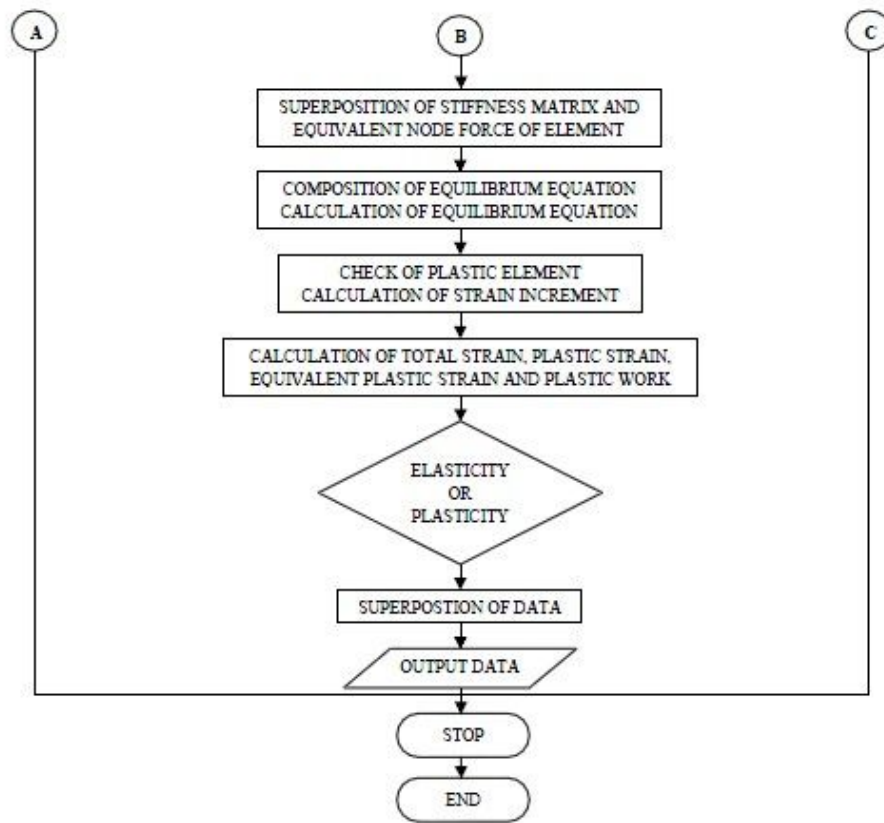


Fig 3.2 Flow diagram for Thermal-Elastic plastic analysis

3.2 Theory of Numerical Simulation

In welding, the heat sources may be considered in such a manner that the effect of radiation and convection are negligible in comparison to the effect of conduction. In the heat conduction analysis the material is assumed to be isotropic and the temperature on the boundary is room temperature.

3.2.1 Heat Conduction Analysis

The spatial and temporal temperature distribution satisfies the following governing equation of un-stationary heat conduction:

$$\rho c \frac{\partial T}{\partial t} = \lambda \left(\frac{\partial^2 T}{\partial x^2} + \frac{\partial^2 T}{\partial y^2} + \frac{\partial^2 T}{\partial z^2} \right) + \dot{Q} \quad (3.1)$$

where T is temperature ($^{\circ}\text{C}$), ρ is density (g/cm^3), \dot{Q} is rate of temperature change due

to heat generation per volume ($\text{cal/cm}^3 \cdot \text{sec}$), t is time (sec), λ is thermal conductivity

of isotropic material ($\text{cal/cm} \cdot \text{sec} \cdot ^{\circ}\text{C}$) and c is specific heat ($\text{cal/g} \cdot ^{\circ}\text{C}$).

To solve this equation of un-stationary heat conduction, following boundary conditions are applied according to the kinds of problem.

- When the temperature is determined on the boundary S_1 :

$$T = \bar{T} \quad (3.2)$$

where \bar{T} is determined temperature.

- When the heat flux, q_o , flows from the boundary S_2 :

$$q = q_o \quad (3.3)$$

- When heat transfer is on the boundary S_3 for convection:

$$q = \alpha_c (T - T_c) \quad (3.4)$$

where α_c is heat transfer coefficient for convection (cal/cm²·sec·°C) , T is boundary

temperature of the object (°C), and T_c is the outside temperature of the object (°C).

- When heat radiation is on the boundary S_4 :

$$q = \sigma F(T^4 - T_r^4) \quad (3.5)$$

where σ is the Stefan Boltzmann constant, F is a compensation coefficient of shape,

and T_r is the temperature of radiation source (°C). This equation can be transformed to

the form of linear equation for the ease of processing as follows:

$$q = \alpha_r(T - T_r) \quad (3.6)$$

where

$$\alpha_r = \sigma F(T + T_r)(T^2 + T_r^2) \quad (3.7)$$

Heat flux, q (cal/cm³·sec·°C), in normal direction on the boundary is derived from the

Fourier law as below:

$$q = -\lambda \frac{\partial T}{\partial n} \quad (3.8)$$

Heat conduction problem for the object of analysis is formulated as the finite element method using Galerkin method. Internal temperature of the element, T , is given by

$$T(x, y, z, t) = [N(x, y, z)]\{\phi(t)\} \quad (3.9)$$

where $[N]$ is a shape function matrix shown the relation between nodal temperature and internal temperature of the element. $\{\phi\}$ is the vector of the nodal temperature of the element at time t .

If Galerkin method is applied in equation (1) using $[N]$ as a weighting function at this time, following equation is obtained.

$$\int_{V^e} [N]^T \left\{ \lambda \left(\frac{\partial^2 T}{\partial x^2} + \frac{\partial^2 T}{\partial y^2} + \frac{\partial^2 T}{\partial z^2} \right) + \dot{Q} - \rho c \frac{\partial T}{\partial t} \right\} dV = 0 \quad (3.10)$$

where superscript, T , shows transformation of matrix and subscript, V^e , shows the domain of element. The term of second order in partial differential equation (3.10) is changed using Green-Gauss theorem, a formula of partial integration, to the following equation.

$$\begin{aligned} & \int_{V^e} \lambda [N]^T \left(\frac{\partial^2 T}{\partial x^2} + \frac{\partial^2 T}{\partial y^2} + \frac{\partial^2 T}{\partial z^2} \right) dV \\ &= - \int_{V^e} \lambda \left(\frac{\partial [N]^T}{\partial x} \frac{\partial T}{\partial x} + \frac{\partial [N]^T}{\partial y} \frac{\partial T}{\partial y} + \frac{\partial [N]^T}{\partial z} \frac{\partial T}{\partial z} \right) dV + \int_{S^e} \lambda [N]^T \left(\frac{\partial T}{\partial n} \right) dS \end{aligned} \quad (3.11)$$

where S^e is the boundary of element.

If equation (3.9) and equation (3.2), Fourier's law, are substituted in equation (3.11), the right side of equation (3.11) becomes as below:

$$= -\int_{V^e} \lambda \left(\frac{\partial[N]^T}{\partial x} \frac{\partial[N]}{\partial x} + \frac{\partial[N]^T}{\partial y} \frac{\partial[N]}{\partial y} + \frac{\partial[N]^T}{\partial z} \frac{\partial[N]}{\partial z} \right) dV \cdot \{\phi(t)\} - \int_{S^e} q[N]^T dS \quad (3.12)$$

Using equation (3.12), equation (3.10) becomes finally as follows:

$$\begin{aligned} & -\int_{V^e} \lambda \left(\frac{\partial[N]^T}{\partial x} \frac{\partial[N]}{\partial x} + \frac{\partial[N]^T}{\partial y} \frac{\partial[N]}{\partial y} + \frac{\partial[N]^T}{\partial z} \frac{\partial[N]}{\partial z} \right) dV \cdot \{\phi(t)\} \\ & - \int_{S^e} q[N]^T dS + \int_{V^e} \dot{Q}[N]^T dV - \int_{V^e} \rho c [N]^T [N] dV \cdot \frac{\partial\{\phi(t)\}}{\partial t} = 0 \end{aligned} \quad (3.13)$$

Simplifying above equation (3.13), un-stationary heat conduction problem can be expressed as following finite element expression for an element.

$$[k]\{\phi\} + [c]\left\{\frac{\partial\phi}{\partial t}\right\} = \{f\} \quad (3.14)$$

where $[k]$, $[c]$ and $\{f\}$ show the heat conductivity matrix of an element, the heat capacity matrix of an element and the heat flow vector of an element, respectively.

They are expressed as follows:

$$[k] = \int_{V^e} \lambda \left(\frac{\partial[N]^T}{\partial x} \frac{\partial[N]}{\partial x} + \frac{\partial[N]^T}{\partial y} \frac{\partial[N]}{\partial y} + \frac{\partial[N]^T}{\partial z} \frac{\partial[N]}{\partial z} \right) dV \quad (3.15)$$

$$[c] = \int_{V^e} \rho c [N]^T [N] dV \quad (3.16)$$

$$\{f\} = \int_{V^e} \dot{Q}[N]^T dV - \int_{S^e} q[N]^T dS \quad (3.17)$$

Boundary conditions on the boundary S_2 to S_4 can be given to substitute q in second term of equation (3.17) using equation (3.3), (3.4) and (3.6).

- When the heat flux, q_o , flows from the boundary S_2 :

From the equation (3.3),

$$\int_{S_2^e} q[N]^T dS = \int_{S_2^e} q_o[N]^T dS \quad (3.18)$$

In the case of adiabatic boundary condition, q_o becomes zero (0).

- When heat transfer is on the boundary S_3 for convection:

$$\text{From the equation (3.4),} \quad \int_{S_3^e} q[N]^T dS = \int_{S_3^e} \alpha_c (T - T_c)[N]^T dS \quad (3.19)$$

If T in the equation (3.19) is substituted by the equation (3.9), the equation (3.19) becomes as below:

$$\int_{S_3^e} q[N]^T dS = \int_{S_3^e} \alpha_c [N]^T [N] dS \cdot \{\phi(t)\} - \int_{S_3^e} \alpha_c T_c [N]^T dS \quad (3.20)$$

- When heat radiation is on the boundary S_4 :

$$\text{From the equation (3.6),} \quad \int_{S_4^e} q[N]^T dS = \int_{S_4^e} \alpha_r (T - T_r)[N]^T dS \quad (3.21)$$

If T in the equation (3.21) is substituted by the equation (3.9), the equation (3.21) becomes as below:

$$\int_{S_4^e} q[N]^T dS = \int_{S_4^e} \alpha_r [N]^T [N] dS \cdot \{\phi(t)\} - \int_{S_4^e} \alpha_r T_r [N]^T dS \quad (3.22)$$

From the above conditions, general boundary condition eliminated first boundary condition when the temperature is determined on the boundary S_1 can be applied to solve the un-stationary heat conduction problem.

Equation (3.15) and (3.17) are modified using equation (3.18), (3.20) and (3.22) as follows:

$$[k] = \int_{V^e} \lambda \left(\frac{\partial [N]^T}{\partial x} \frac{\partial [N]}{\partial x} + \frac{\partial [N]^T}{\partial y} \frac{\partial [N]}{\partial y} + \frac{\partial [N]^T}{\partial z} \frac{\partial [N]}{\partial z} \right) dV + \int_{S_3^e} \alpha_c [N]^T [N] dS + \int_{S_4^e} \alpha_r [N]^T [N] dS \quad (3.23)$$

$$\{f\} = \int_{V^e} \dot{Q}[N]^T dV - \int_{S_2^e} q_0[N]^T dS + \int_{S_3^e} \alpha_c T_c [N]^T dS + \int_{S_4^e} \alpha_r T_r [N]^T dS \quad (3.24)$$

Therefore, finite element formula of an element can be derived as a form of matrix equation including boundary conditions by using equation (3.16), (3.23) and (3.24).

Finite element formula for the whole object analysed is constructed with assembled each matrix of elements and it can be expressed as follows:

$$[K]\{\Phi\} + [C]\left\{\frac{\partial \Phi}{\partial t}\right\} = \{F\} \quad (3.25)$$

where $[\Phi]$, $[K]$, $[C]$ and $\{F\}$ show the vector of the nodal temperature in the whole object, the heat conductivity matrix in the whole object, the heat capacity matrix in the whole object and the heat flow vector in the whole object, respectively. They are given as below.

$$[\Phi] = \sum_e \phi, \quad [K] = \sum_e k, \quad [C] = \sum_e c, \quad \{F\} = \sum_e f \quad (3.26)$$

3.2.2 Thermal elasto-plastic analysis

Basic theory for thermal stress analysis by finite element method

The increment of strain in the element is given by appropriate differentiation of the internal displacements as given below.

$$\{d\varepsilon\} = [B]\{dw\} \quad (3.27)$$

The increment of stress in element is obtained by using an appropriate matrix $[D]$, the elasticity matrix $[D^e]$ or the plasticity matrix $[D^p]$ and the increment of strain.

$$d\sigma = [D]\{d\varepsilon\} \quad (3.28)$$

If the increment of initial strain $\{d\varepsilon_0\}$ exists, increment of stress is expressed as follows.

$$\{d\sigma\} = [D]\{d\varepsilon - d\varepsilon_0\} \quad (3.29)$$

where the initial strains are function of temperature such as thermal strains and has the following relation.

$$\{d\varepsilon_0\} = \{d\varepsilon^T\} = \{\alpha\}dT \quad (3.30)$$

Using this relation, the increment of stress, equation (3.29), can be rewritten in the following form.

$$\{d\sigma\} = [D]\{d\varepsilon\} - [C]dT \quad (3.31)$$

The relationship between the increment of the nodal force, $\{dF\}$, and the nodal displacement, $\{dw\}$, is obtained by applying the principle of virtual work as below.

$$\{dF\} = \int [B]^T [D] \{d\varepsilon\} dV - \int [B]^T [C] dT dV = [K] \{dW\} - \{dL\} \quad (3.32)$$

$$\text{Where, } [K] = \int [B]^T [D] \{d\varepsilon\} dV \text{ is the stiffness matrix} \quad (3.33)$$

$$\{dL\} = \int [B]^T [C] dT dV \text{ is the nodal force due to initial strain} \quad (3.34)$$

The equilibrium state of the whole object will be kept in satisfying the additional equilibrium condition at each step of temperature increments which are constituted with individual equilibrium equation at each node as follows.

$$\sum \{dF\} = \sum [K] \{dW\} - \sum \{dL\} \quad (3.35)$$

If there is no external force acting at the nodes, the above equation is expressed in the simple form as below.

$$\sum \{dL\} = \sum [K] \{dw\} \quad (3.36)$$

3.2.3 Temperature dependency of stress and strain

Stress-strain relation in elastic range

In the elastic range, the increment of total strain consists of increment of elastic strain $\{d\varepsilon^e\}$ and the increment of thermal expansion strain $\{d\varepsilon^T\}$ and is related as

$$\{d\varepsilon\} = \{d\varepsilon^e\} + \{d\varepsilon^T\} \quad (3.37)$$

The increment of thermal expansion strain is expressed using the coefficient of linear expansion.

$$\{d\varepsilon^T\} = \{\alpha\}dT \quad (3.38)$$

When the elasticity matrix, $[D^e]$, changes as temperature increase, the increment of elastic strain is given in the following form.

$$\begin{aligned} \{d\varepsilon^e\} &= [D^e]^{-1}\{d\sigma\} + \frac{\partial[D^e]^{-1}}{\partial T}\{\sigma\}dT \\ &= \{d\varepsilon^e\} + \{d\varepsilon^{T^1}\} \end{aligned} \quad (3.39)$$

Transposing $\{d\sigma\}$ in above equation, the increment of stress is given by

$$\{d\sigma\} = [D^e]\{d\varepsilon^e\} - [D^e]\frac{\partial[D^e]^{-1}}{\partial T}\{\sigma\}dT \quad (3.40)$$

Substituting equation (3.39) into equation (3.37), the increment of strain is given

$$\text{by } \{d\varepsilon\} = [D^e]^{-1}\{d\sigma\} + \frac{\partial[D^e]^{-1}}{\partial T}\{\sigma\}dT + \{\alpha\}dT \quad (3.41)$$

Substitution of equation (3.38) and (3.41) into equation (3.40) becomes

$$\{d\sigma\} = \underbrace{[D^e]}_{[D]}\{d\varepsilon\} - \underbrace{[D^e]\left(\{\alpha\} + \frac{\partial[D^e]^{-1}}{\partial T}\{\sigma\}\right)}_{[C]}dT = [D^e]\{d\varepsilon^e\} \quad (3.42)$$

From this equation, the required matrix $[D]$ and $[C]$ in equation (3.31) is obtained.

2) Stress-strain relation in plastic range.

Materials yield when its yield function, f , satisfy the equation

$$f = 0 \quad (3.43)$$

According to incremental theory of plasticity (flow rule), the increment in plastic strains, $\{d\varepsilon^p\}$, is given in following form.

$$\{d\varepsilon^e\} = \lambda \left\{ \frac{\partial f}{\partial \sigma} \right\} \quad (3.44)$$

where f is the plastic potential and λ is a positive scalar.

In the elasto-plastic problem, the total increment of strain is the summation of increment in elastic strains, plastic strains and thermal strains as follows.

$$\{d\varepsilon\} = \{d\varepsilon^e\} + \{d\varepsilon^p\} + \{d\varepsilon^T\} \quad (3.45)$$

substituting (B13) in above equation

$$\{d\varepsilon\} = \{d\varepsilon^{e^1}\} + \{d\varepsilon^p\} + \{d\varepsilon^T\} + \{d\varepsilon^{T^1}\} \quad (3.46)$$

Then equation (B14) becomes,

$$\{d\sigma\} = [D^e](\{d\varepsilon\} - \{d\varepsilon^p\} - \{d\varepsilon^T\}) - [D^e] \frac{\partial [D^e]^{-1}}{\partial T} \{\sigma\} dT \quad (3.47)$$

Therefore,

$$\{d\sigma\} = [D^e]\{d\varepsilon\} - [D^e]\lambda \left\{ \frac{\partial f}{\partial \sigma} \right\} - [D^e] \left(\{\alpha\} + \frac{\partial [D^e]^{-1}}{\partial T} \{\sigma\} \right) dT \quad (3.48)$$

If the material is under loading in the plastic range, the following condition should be satisfied

$$0 = df = \left\{ \frac{\partial f}{\partial \sigma} \right\}^T \{d\sigma\} + \left\{ \frac{\partial f}{\partial \varepsilon^p} \right\}^T \{d\varepsilon^p\} + \frac{\partial f}{\partial T} dT \quad (3.49)$$

Substituting (3.48) in to equation (3.49)

$$\begin{aligned} 0 = df = & \left\{ \frac{\partial f}{\partial \sigma} \right\}^T \left(\{d\sigma\} = [D^e]\{d\varepsilon\} - [D^e]\lambda \left\{ \frac{\partial f}{\partial \sigma} \right\} - [D^e] \left(\{\alpha\} + \frac{\partial [D^e]^{-1}}{\partial T} \{\sigma\} \right) dT \right) \\ & + \left\{ \frac{\partial f}{\partial \varepsilon^p} \right\}^T \lambda \left\{ \frac{\partial f}{\partial \sigma} \right\} + \frac{\partial f}{\partial T} dT \end{aligned} \quad (3.50)$$

Rearranging the above equation,

$$\lambda = \frac{\left\{ \frac{\partial f}{\partial \sigma} \right\}^T [D^e]\{d\varepsilon\} - \left\{ \frac{\partial f}{\partial \sigma} \right\}^T [D^e] \left(\{\alpha\} + \frac{\partial [D^e]^{-1}}{\partial T} \{\sigma\} \right) dT + \frac{\partial f}{\partial T} dT}{\left\{ \frac{\partial f}{\partial \sigma} \right\}^T [D^e] \left\{ \frac{\partial f}{\partial \sigma} \right\} - \left\{ \frac{\partial f}{\partial \varepsilon^p} \right\}^T \left\{ \frac{\partial f}{\partial \sigma} \right\}} \quad (3.51)$$

From the substitution of above equation into equation (3.48), equation (3.48) is rearranged as follows and it shows the relation between the increments of stress and total strain in the plastic range.

$$\{d\sigma\} = [D^e] \{d\varepsilon\} - \left([D^p] \{\alpha\} + [D^p] \frac{\partial [D^e]^{-1}}{\partial T} \{\sigma\} + [D^e] \left\{ \frac{\partial f}{\partial \sigma} \right\} \frac{\partial f}{\partial T} \bigg/ S \right) dT \quad (3.52)$$

where $[D^p]$ is the plasticity matrix and is expressed as

$$\text{below. } [D^p] = [D^e] - [D^e] \left\{ \frac{\partial f}{\partial \sigma} \right\} \left\{ \frac{\partial f}{\partial \sigma} \right\}^T [D^e] \bigg/ S \quad (3.53)$$

$$S = \left\{ \frac{\partial f}{\partial \sigma} \right\}^T [D^e] \left\{ \frac{\partial f}{\partial \sigma} \right\} - \left\{ \frac{\partial f}{\partial \varepsilon^p} \right\}^T \left\{ \frac{\partial f}{\partial \sigma} \right\} \quad (3.54)$$

Then, the required matrix $[D]$ and $[C]$ to solve the equation (3.31) are shown to be

$$[D] = [D^p] \quad (3.55)$$

$$[C] = [D^p] \{\alpha\} + [D^p] \{\alpha\} + [D^p] \frac{\partial [D^e]^{-1}}{\partial T} \{\sigma\} + [D^e] \left\{ \frac{\partial f}{\partial \sigma} \right\} \frac{\partial f}{\partial T} \bigg/ S \quad (3.56)$$

When λ is found to be negative ($\lambda < 0$) during the computation, the material is subjected to unloading.

At this condition, the increment relation of stress and strain should be replaced by equation (3.42) instead of equation (3.52).

In the thermo-mechanical analysis, the incremental theory of plasticity is employed. The plastic deformation of the materials is assumed to obey the von Mises yield criterion and the associated flow rule. The relationship of the rate components between thermal stresses, σ_{ij} , and strains, ε_{ij} , is described by

$$\varepsilon_{ij} = \frac{1+\nu}{E}\sigma_{ij} - \frac{\nu}{E}\sigma_{kk}\delta_{ij} + \lambda s_{ij} + \left[\alpha + \frac{\partial \alpha}{\partial T}(T - T_0) \right] \dot{T} \quad (3.57)$$

where E is the Young's modulus, ν is the Poisson's ratio, α is the thermal expansion coefficient,

$$s_{ij} = \sigma_{ij} - \frac{1}{3}\sigma_{kk}\delta_{ij} \quad (3.58)$$

are the components of deviatoric stresses and λ is the plastic flow factor. $\lambda=0$ for elastic deformation or $\sigma_e < \sigma_s$, and $\lambda > 0$ for plastic deformation or $\sigma_e \geq \sigma_s$, here σ_s is the yield stress and is the

$$\sigma_e = \left[\frac{3}{2} s_{ij} s_{ij} \right]^{1/2} \quad (3.59)$$

is the von Mises effective stress.

It is well known that the thermo-mechanical analysis for welding simulation using finite element method is extremely time-consuming. To reduce computational time and still maintain reasonable accuracy, many thermo-mechanical numerical analyses use a “cut-off temperature”, i.e. the mechanical properties above the cut-off temperature are assumed to maintain constant values.

To further save computational time without loss accuracy of solutions, different time steps are used for the two un-coupled analyses, i.e. 0.1 s for the heat transfer analysis and 1.0 s for the stress-deformation analysis. Overall, the actual PC's time in a typical simulation is about 3.5 min for the temperature analysis, and 120 min for the stress and deformation analysis.

3.3 Data transferring between commercial software and developed program

In many cases a significant percentage of the time spent on FEM analysis is devoted to pre-processing and post processing stage. This is the case for numerous FEM codes used in specialized researches. In the present work, an interface is built using the high level language PCL (PATRAN Command Language) that can be compiled directly from PATRAN desktop. Hence, PATRAN can be used as pre-processor and post processor for the developed codes. Three PCL programs were developed. First is WELD.pcl, used to transfer coordinate and connectivity details of the model developed in PATRAN to in-house solver. Second is BC1.pcl, used to transfer the details of the surface elements to in-house solver and the last one is MODEL.pcl, used to export the result from in-house solver to commercial package for further analysis with the external load. In this work, only first two PCL programs were used as there is no external loading connected with the experiment. Using the formulation discussed in Section 3.1, finite element codes are developed for heat transfer and residual stress analysis of dissimilar joint. The developed code consists of 28 subroutines for heat transfer analysis and 47 subroutines for residual stress analysis. According to the task performed; the subroutines can be grouped accordingly as shown in Fig3.3 and Fig 3.4.

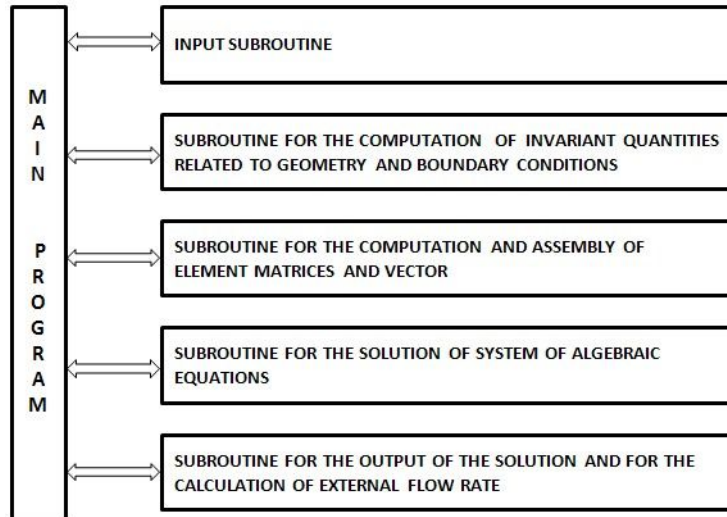


Fig 3.3 Structure of the heat transfer analysis program

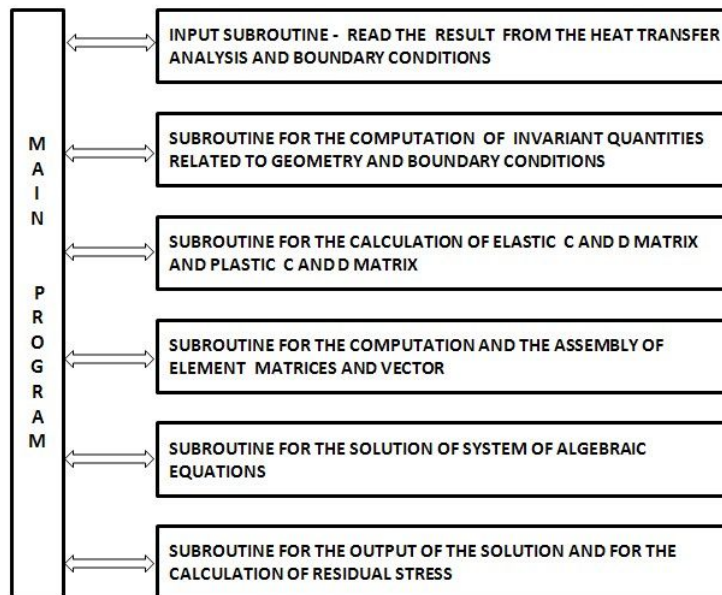


Fig 3.4 Structure of the residual stress analysis program

Chapter 4

FEA AND EXPERIMENTAL METHOD

FOR TAFSW

4.1 Finite Element Analysis model

The finite element model for the heat transfer analysis of dissimilar joint for particular tool geometry and material properties (Fig.4.1) is developed based on the heat transfer model described in previous work [28]. To obtain heat input model, volume of the tool is deducted from the weld nugget zone and the die cavity volume is deducted from extrusion zone. Tool-work piece contact location in the analysis model is taken same as in experiment. Al 6061-T6 and STS 304/SS400 with principal dimension 100mm×40mm×3mm is selected for numerical analysis. A non-uniform mesh with solid brick element has been used for modeling and sufficient fine mesh size is generated at the weld region to get more accurate results. For integration, time step of

1second is adopted. The boundary conditions of the FE model are taken same as those of the experimental condition. It is assumed that the material is isotropic and the temperature at the boundary is room temperature. A convective coefficient of $30\text{W}\cdot\text{m}^{-2}\cdot^{\circ}\text{C}^{-1}$ and $25\text{W}\cdot\text{m}^{-2}\cdot^{\circ}\text{C}^{-1}$ is used for aluminium and stainless steel alloys respectively at top and side surfaces which are typical for natural convection between parent materials and air [18] [40]. The percentage slip is assumed between 0.1-0.8 [23, 42]. The tool exerts a vertical force of 5.5kN during welding process. From this, a uniform contact pressure at tool/work piece interface is calculated.

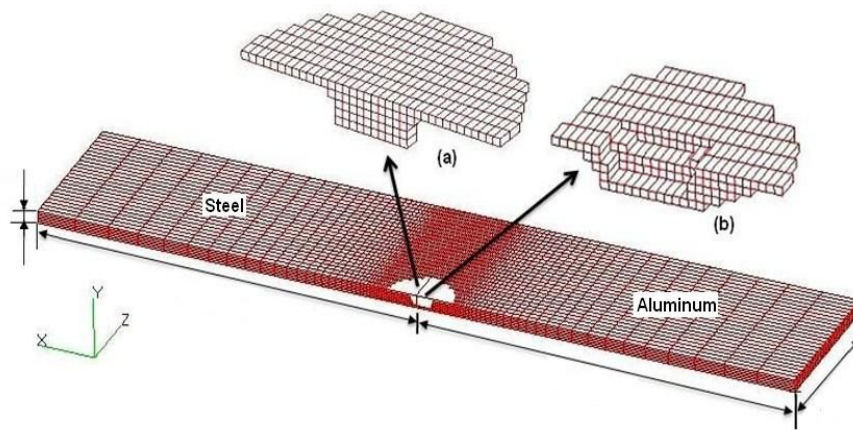


Fig. 4.1 FE model for heat conduction analysis

(a) Tool volume (b) Heat input volume around the tool

At steel side, the quantity of heat input from the TIG arc is added to the heat input from FSW process based on super position principle. The heat flux for heat input element is calculated by multiplying element volume and uniform heat flux per volume. Uniform heat flux is obtained by dividing total heat energy by the product of heat input volume and heating time per unit welding length.

For the thermal-stress problem, the temperature distribution of un-steady state heat transfer problem for continuance object is first obtained. The heat transfer problem which changes with time depends on temperature change, and is treated as the initial strains. Since the physical property of the material that makes up each element changes with time, the force–displacement relation on nodal points was constructed considering the above conditions. In order to generally analyse weld stress, the temperature dependency of materials through the elastic and plastic region was considered, assuming that the material is isotropic. In the plastic region, Von-mises yield-criteria were used as a yield point function with the linear-isotropic hardening-rule.

4.1.1 Coefficient of friction

The coefficient of the friction is believed to vary during the FSW process; the detail of the variation is still not clear so far. The value of friction coefficient is assumed as constant in many previous literatures as shown in Table 4.1. An effective temperature dependent coefficient of friction, which is also used in FSW of steel joint [51], is assumed in this study based on the reference shown in Table 4.2.

Table 4.1 Coefficient of friction considered in various FSW numerical studies

Authors'	Coefficient of friction, μ (Remarks)
Song and Kovacevic [45] Xu et al.[46]	0.4 and 0.3 for Aluminum alloy and tool steel
Schmidt and Hattel [47]	0.3 for Al 2024-T3
Song et al. [48]	0.5 at 300K and linearly decrease to 0.3 at melting point of Aluminum

Frigaard et al. [49]	Adjusted the value μ to keep maximum temperature not to exceed melting point
----------------------	--

Table 4.2 Temperature dependent friction coefficient of aluminum and steel [50]

Temperature (°C)	22.0	34.7	93.3	147.5	210.6	260.0	315.6	371.1	426.7	582.0
Friction Coefficient (μ)	0.610	0.545	0.259	0.115	0.064	0.047	0.035	0.020	0.007	0

Temperature dependent material properties such as thermal conductivity, density, coefficient of thermal expansion, specific heat and yield stress for Al 6061-T6 and STS304 at all the elastic–plastic zones are considered in this analysis [30].

The temperature field obtained from the heat conduction analysis program was input as the body force to residual stress program to analyse residual stress characteristics.

4.2 Experimental method

Gantry type WINXEN FSW system having maximum load capacity 3000kgf, together with DAIHEN inverter ELECON 500P TIG welding machine was used for TAFSW welding experiment. To prevent overheating of aluminium and obtain successful weld, pin was offset to the aluminium side just penetrating steel. Dimensions of the dissimilar plates and relative location of tool pin with the butt line are given in Fig.4.2 Tungsten carbide (WC-Co12%) tool having shoulder diameter 18mm, pin top

diameter 6.5mm and pin bottom diameter 5.5mm was used in the experiment. TIG leading FSW tool is implemented, where distance between TIG electrode and FSW tool was 16mm and applied tool force was 5.5kN. Welding trials were conducted to determine the appropriate welding parameters under various processing conditions. The specification of tungsten carbide tool used in the experiment is shown in Table 4.3. The preheating condition and optimum welding conditions obtained from the experiment is given in Table 4.4 and Table 4.5 respectively.

Table 4.3 Specification of tool used for TAFSW

Co ($\pm 0.5\%$)	Grade	WC ($\pm 0.5\%$)	Grain Size(μm)	Density (g/cc)	Hardness (HV30)
12%	WF20	88%	0.6	14.15	1670

Table 4.4 Optimum condition for TIG preheating



Shield Gas : Ar - 5ℓ/min. wire : Φ 1.6mm				
No.	Current	Pulsed Current	Welding speed	Torch angle
1	140A	40A	2mm/s	40°
Macro				Width : 4mm Depth : 2.2mm
Shield Gas : Ar - 10ℓ/min. wire : Φ 2.4mm				
No.	Current	Pulsed Current	Welding speed	Torch angle
2	70A	70A	1mm/s	60°
Macro				Width : 1.5mm Depth : 1.6mm

Table 4.5 Welding condition for TAFSW

Welding conditions		
TIG	Pulse Current/pulsed time	80A/0.2s
	Base Current/pulsed time	70A/0.5s
	Arc voltage	26 V

	Gas flow rate (Argon)	7 ~ 10 ℓ/min
	Arc length	2mm
	Electrode angle	60°
	Dia. of electrode	2.4mm
FSW	Rotation speed	300 rpm
	Welding speed	0.8 mm/s (STS304) 1.0 mm/s (SS400)
	Shoulder dia.	Ø18 mm
	Top pin dia.	Ø6.5 mm
	Bottom pin dia.	Ø5.5 mm
	Room temperature	20°C

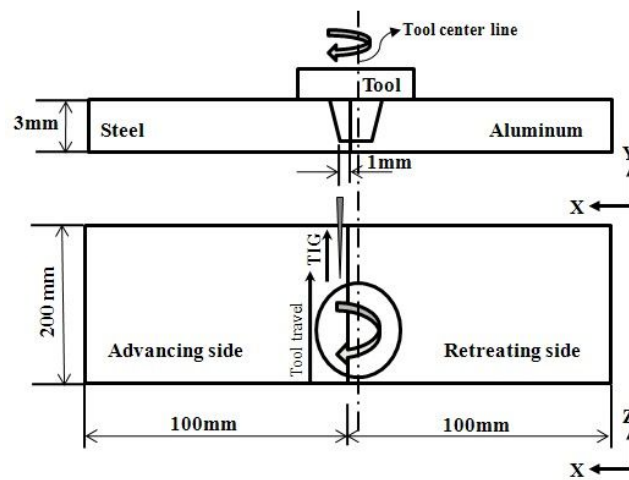
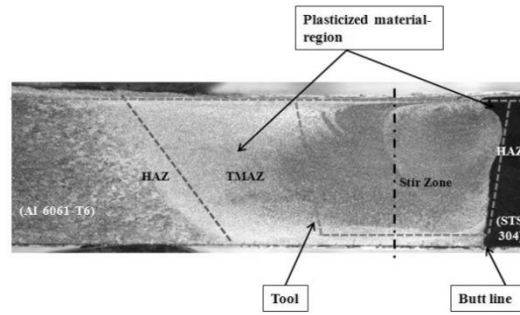
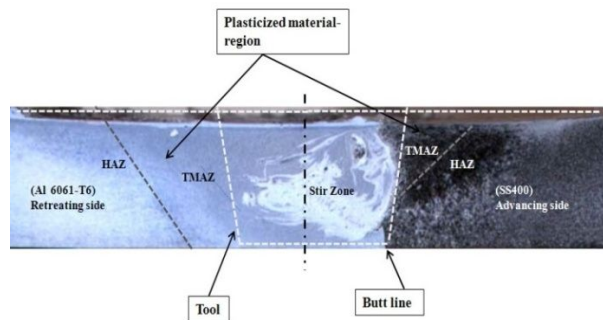


Fig. 4.2 Tool work piece geometry for TAFSW experiment



a) Al 6061-ST304













b) Al6061- SS400

Fig. 4.3 Weld cross-section of dissimilar welded joint by TAFSW


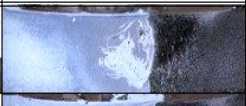








The image of the cross-section and top surface of weld obtained with optimised welding condition is shown in Fig.4.3. The stirring action took place mainly in the aluminium side because of the tool location with workpiece. The weld nugget exhibits a classical onion ring structure on the transverse section of aluminium alloy. Bead surface and cross section of dissimilar butt joint by TAFSW at various welding speed is shown in Fig 4.4 and Fig.4.5 respectively.

The welded joint is visually examined and machined into standard test specimen. Room-temperature tensile tests as per ASTM E8 were conducted on three weld specimens made with optimised parameters and a maximum tensile strength of

290MPa was obtained which is about 93% of Al6061-T6 base metal tensile strength (310MPa).

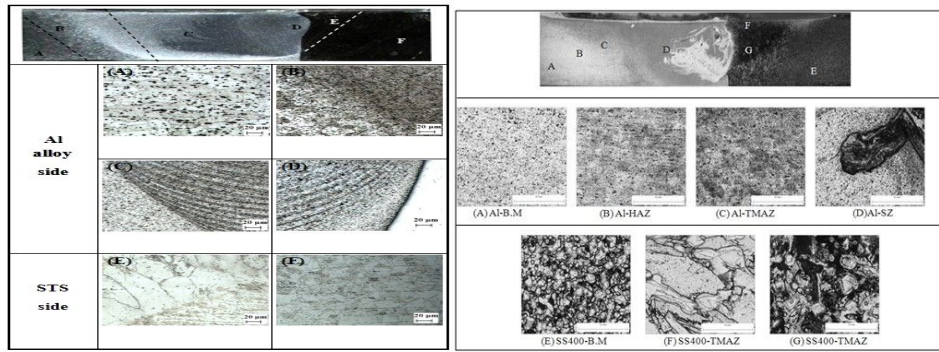
RPM	Travel speed	Bead appearance	Macro image
400	0.6		
	0.8		
500	0.6		
	0.8		
	1.0		

a) Al 6061-ST304 dissimilar joint

RPM	Travel speed	Appearance	Macro image
300	1.0		
	1.2		
	1.4		
400	1.0		
	1.4		

b) Al6061- SS400 dissimilar joint

Fig 4.4 Bead surface and cross section of dissimilar butt joint by TAFSW



a) Al 6061-STS304

b) Al6061- SS400

Fig 4.5 Microstructure images of TAFSW dissimilar butt joint

4.2.1 Experimental measurement of temperature

Transient temperatures at mid thickness were recorded at six locations during the TAFSW process using K type thermocouples of 1mm diameter inserted into 1.5mm diameter holes drilled on top side of work specimens (Fig.4.4). Thermocouples placed to intersect the stir zone region often are crushed or displaced by the deforming material of the stir zone before reaching peak temperatures, thereby introducing uncertainties in measurement. In addition, thermocouples attached to the top surface of the workpiece close to the edge of the stir zone are often severed by extrusion of the flashing from under the tool shoulder before reaching peak temperatures. To circumvent this problem, thermocouples were attached to the workpiece in holes at several locations on the top surface in this study.

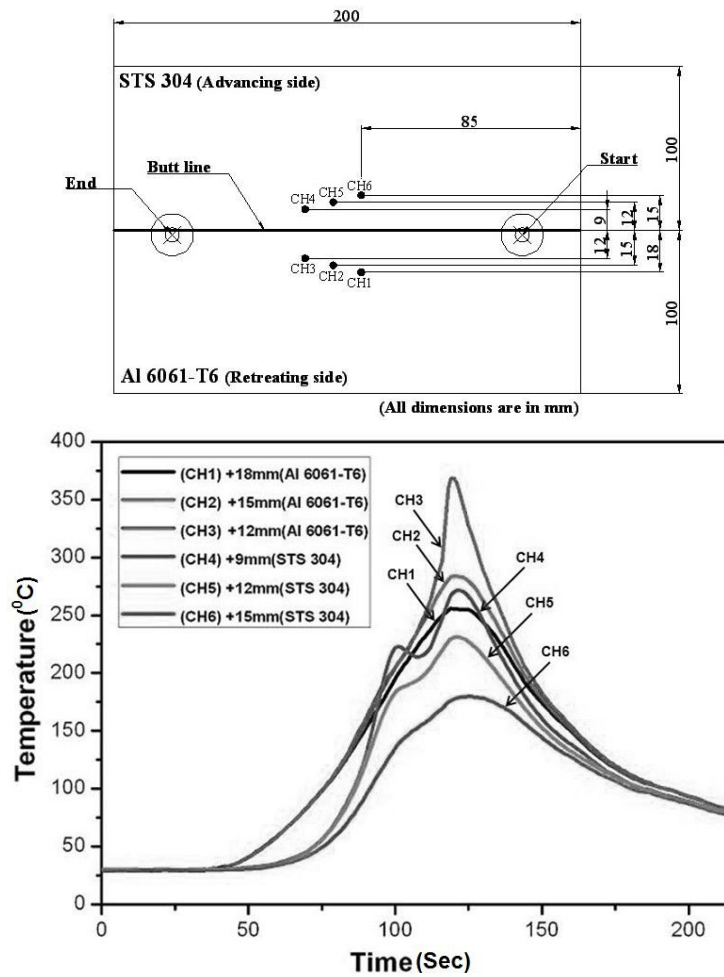


Fig. 4.6 Location of thermocouples and corresponding variation of transient temperature in Al-STS 304 dissimilar butt joint (for optimum welding condition)

Using infrared (IR) camera, instantaneous temperature at the surface of the workpiece during TAFSW process was measured and the temperature field generated is shown in (Fig.4.7).

The temperature measured using thermocouples for dissimilar joint of Al 6061 and SS400 by conventional FSW and TAFSW are shown in Fig.4.8.

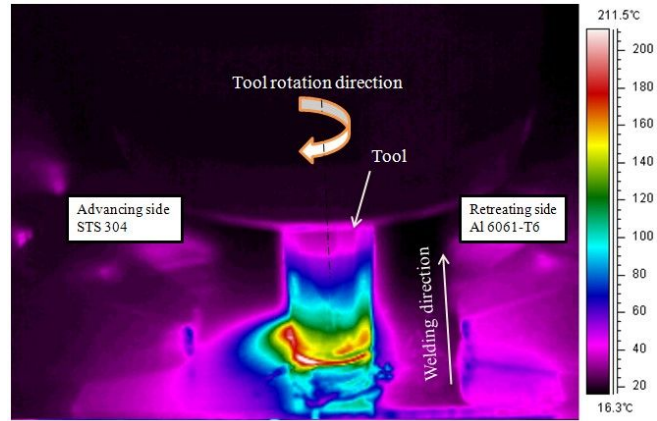


Fig. 4.7 IR camera image showing surface temperature during TAFSW

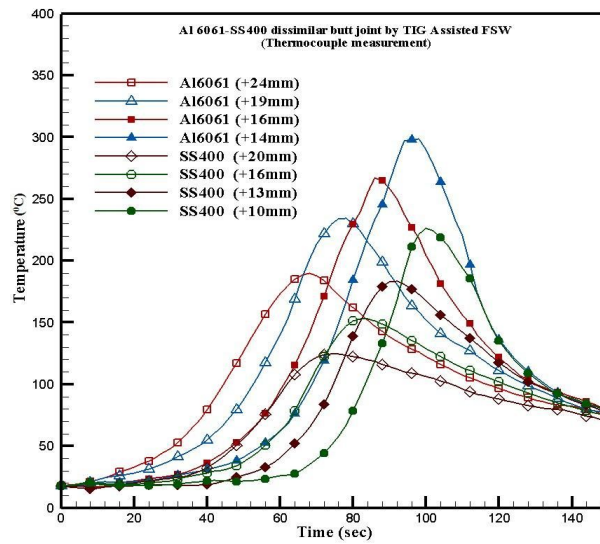


Fig. 4.8 Variation of transient temperature in

Al-SS400 dissimilar butt joint (for optimum welding condition)

4.2.2 Measurement of Residual stress

The surface residual stress developed in dissimilar weld is measured using a strain gauge (Fig.4.9) as proposed by Ueda [40]. In this method two strain-relaxation measurements are performed, one from block to thin slice and other from slice to small die, each with a strain gauge. The slice to die data was used to determine the Eigen

strain components in the transverse perpendicular plane and block to slice data for Eigen strain components determination in longitudinal direction. The locations of strain gauges to measure residual stress are shown in below Figure.

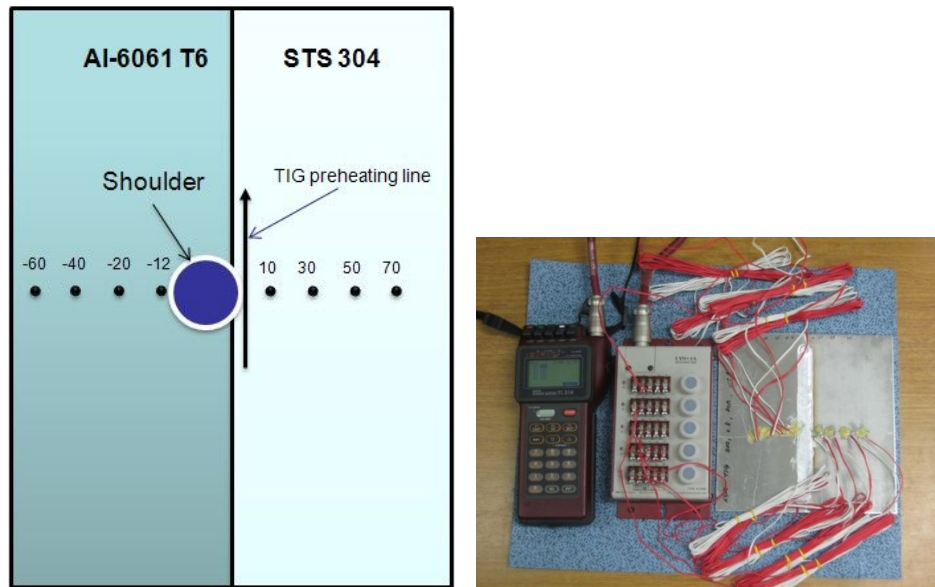


Fig 4.9 Experimental measurement of residual stress and locations of strain gauges
(in mm) away from weld center line

Table 4.4 shows the measured values of residual stress using strain gauge at different locations in Al6061-ST304 TAFS welded specimen.

Table 4.6 Residual stress values of dissimilar butt joint by TAFSW

	Retreating side (Al6061)				Advancing side (STS304)			
Strain gauge locations from center	-60	-40	-20	-12	10	30	50	70
Residual stress (MPa)	15	-10	35	17	7	39.2	-20	-18.7

Chapter 5

RESULTS AND DISCUSSIONS

5.1 Heat conduction analysis

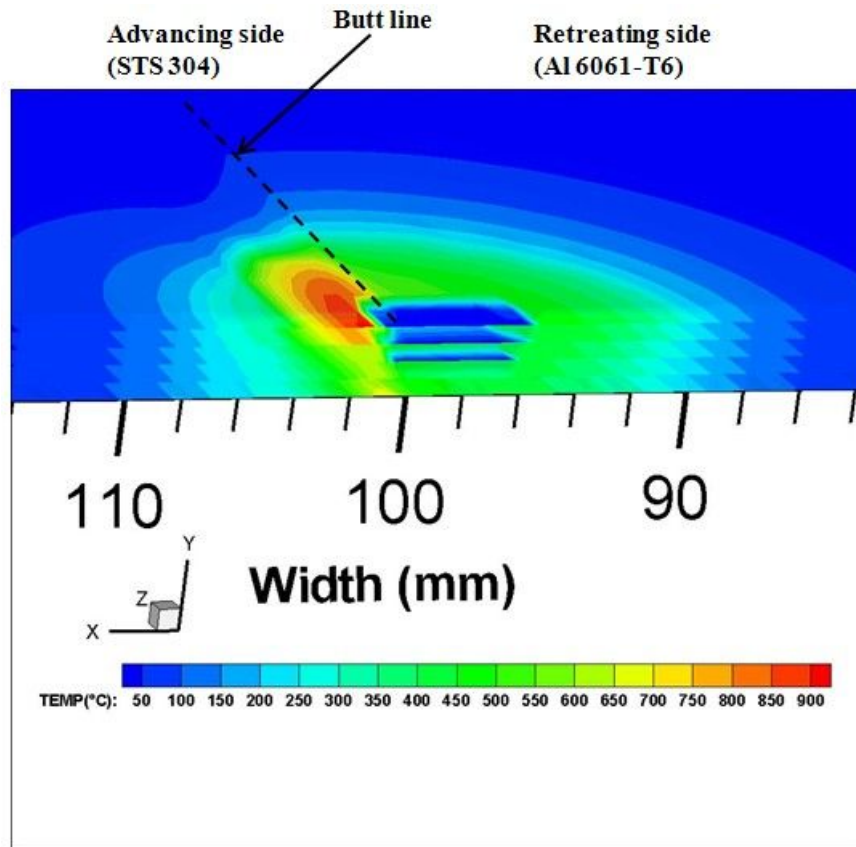
5.1.1 Aluminum 6061-STS304 dissimilar butt joint

The section plot of transient temperature distribution contour, along the weld length and thickness, obtained from the three dimensional heat transfer analysis of dissimilar joint by TAFSW is shown in Fig 5.1. The temperature fields are measured at 2sec after welding, at which the maximum heating temperature occurs. Fig 5.2 shows the distribution of temperature from FEA calculations along the transverse direction of the work specimens at welding time of 2 seconds for the rotational speed of 300 rpm.

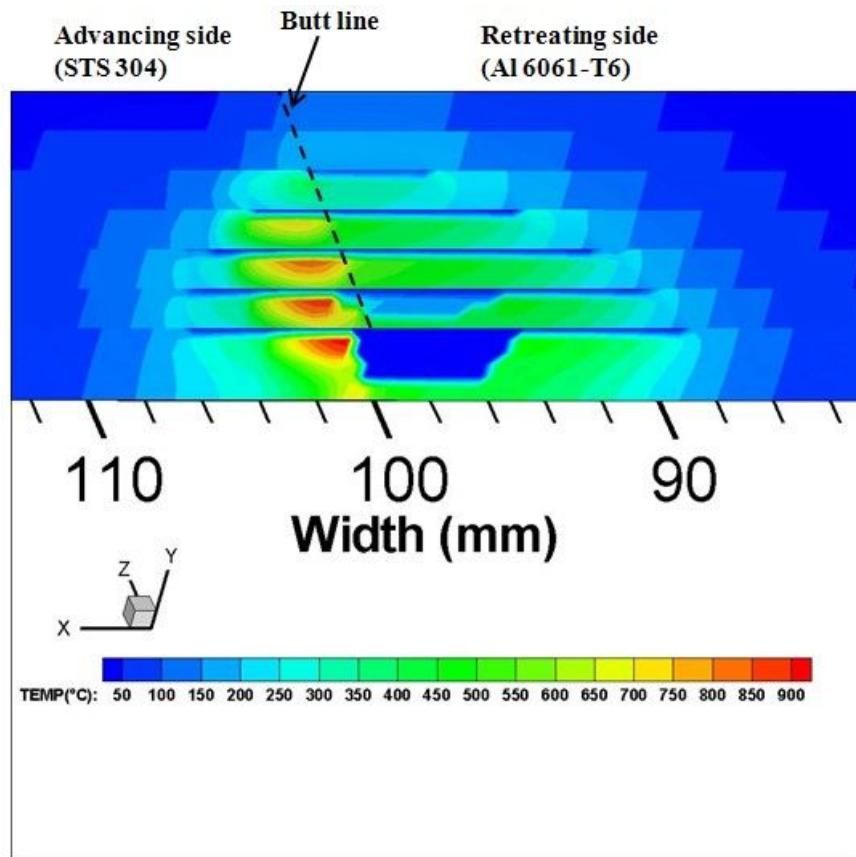
At the region of maximum temperature in STS 304, plastic deformation is expected to be stronger and assumed to extend half the specimen thickness as clearly more visible on bulge part of interface as shown in Fig 4.3. This could be because its plastic state induced primarily by pre-heating temperature. Hence it can be inferred that shoulder driven material flow is more intense in steel due to higher preheating temperatures, making steel to flow towards aluminium on top half thickness of interface. This in return will enhance material behavior and improve the material bonding without the need of higher torque of FSW.

One of the other phenomena observed is during welding, the highest temperature is observed just below the shoulder near stir zone. The maximum simulated temperature at the thermo-mechanically affected zone (TMAZ) in steel occurs at advancing side is about 930°C . In case of aluminium alloy maximum temperature occurs at retreating side and is about 474°C . Due to reduction in material area below tool pin, more heat is conducted at pin bottom than at pin sidewalls. The temperature near the joint line of the pin bottom comes to around 581°C . Aluminium conducts heat more at this contact region and slightly tends to melt at the bottom joint line. The heat flow is found wider towards aluminium due to its high heat conductive

characteristic compared to steel. The heat affected zone (HAZ) temperatures are 558°C and 296°C for steel and aluminium respectively.



a) temperature distribution along weld length



b) temperature distribution along thickness

Fig. 5.1 Temperature contour along weld length and thickness obtained at 2sec for Al6061-ST304 butt joint

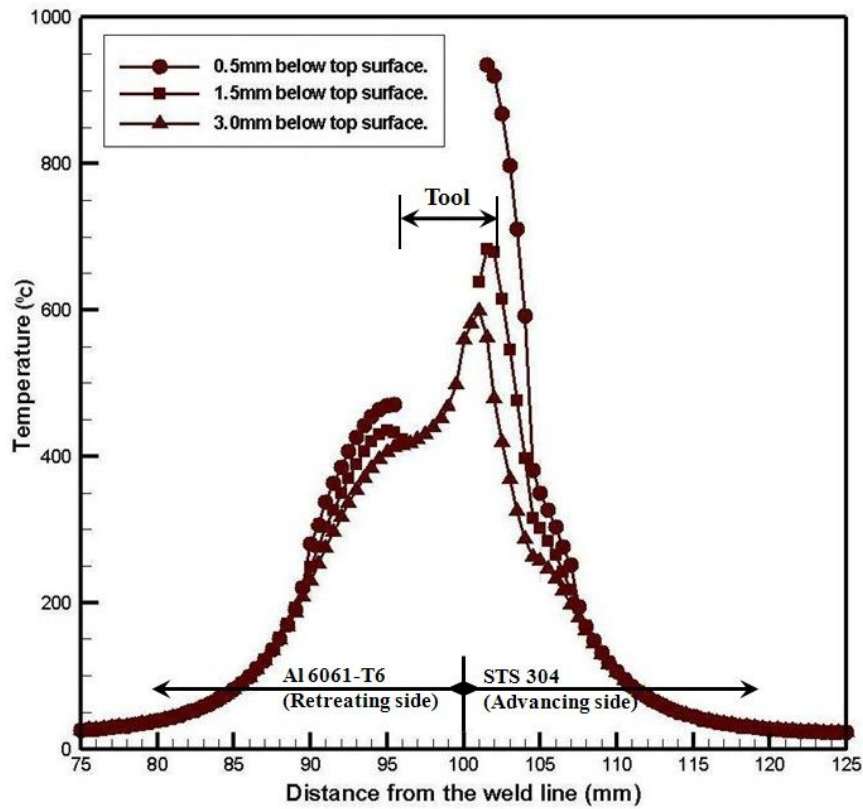
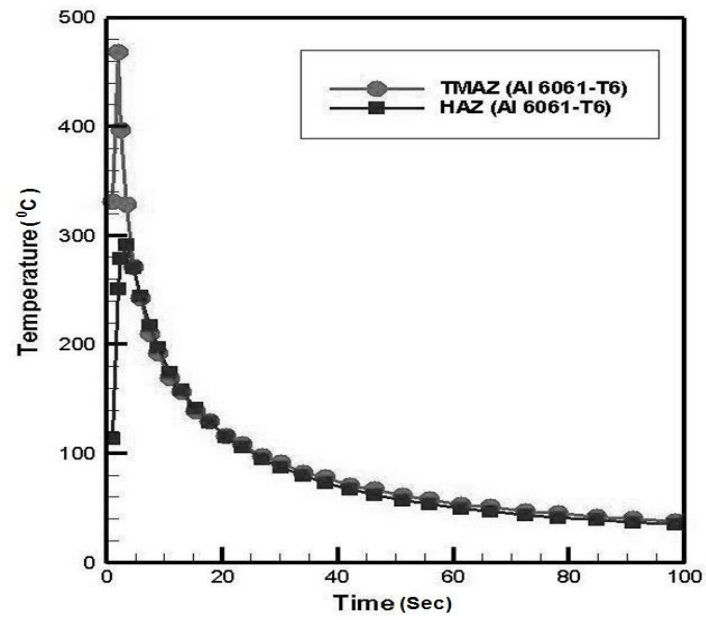
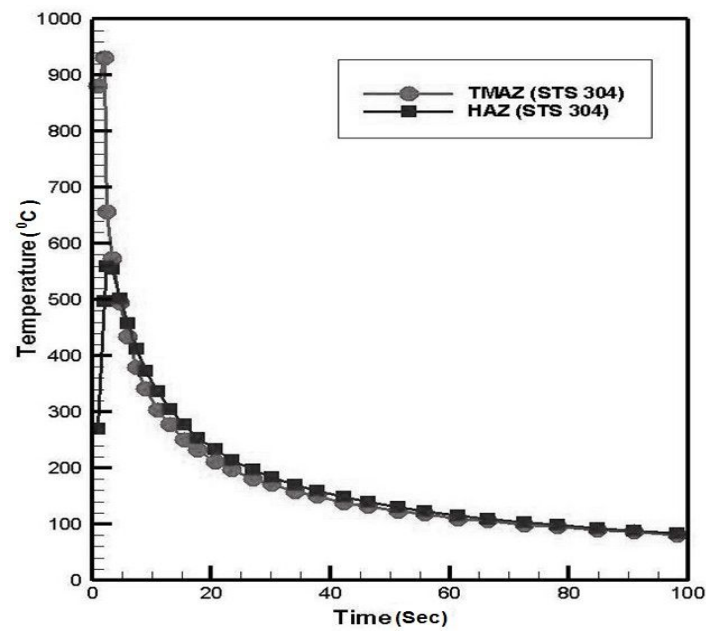


Fig. 5.2 Distribution of temperature at 2 seconds along transverse direction in Al6061-STSS304 butt joint

The temperature history at the point of maximum temperature at TMAZ and HAZ in dissimilar joint is shown in Fig 5.3. From the figure it can be inferred that due to the lower thermal conductivity and lower specific heat of STS 304, most heat is hold in STS 304 compared to Al 6061-T6.



(a) retreating side (Al6061-T6)



(b) advancing side (STS304)

Fig 5.3 Time-Temperature plot for Al 6061-ST304 dissimilar joint by TAFSW

5.1.2 Aluminum 6061-SS400 dissimilar butt joint

Three dimensional transient temperature distribution contours, along the weld length and thickness, obtained from the heat transfer analysis of dissimilar joint by TAFSW are shown in Fig 5.4. The temperature fields are measured at 2sec after welding, at which the maximum heating temperature occurs. The maximum simulated temperature at the thermo-mechanically affected zone (TMAZ) in steel occurs at advancing side is about 884⁰C. In case of aluminium alloy maximum temperature occurs at retreating side and is about 459⁰C. The calculated HAZ temperatures are 490⁰C and 380⁰C for steel and aluminum respectively. The maximum temperature occurred at tool bottom is about 480⁰C. The heat flow is found wider towards aluminium due to its high heat conductive characteristic compared to steel. But the temperature flow is not severely restricted by steel compared to Al-STS304 joint, where heat flow is highly restricted by STS304. The cooling time for SS400 is slower than that of STS 304. The temperature history at the point of maximum temperature at TMAZ and HAZ in dissimilar joint is shown in Fig 5.5.

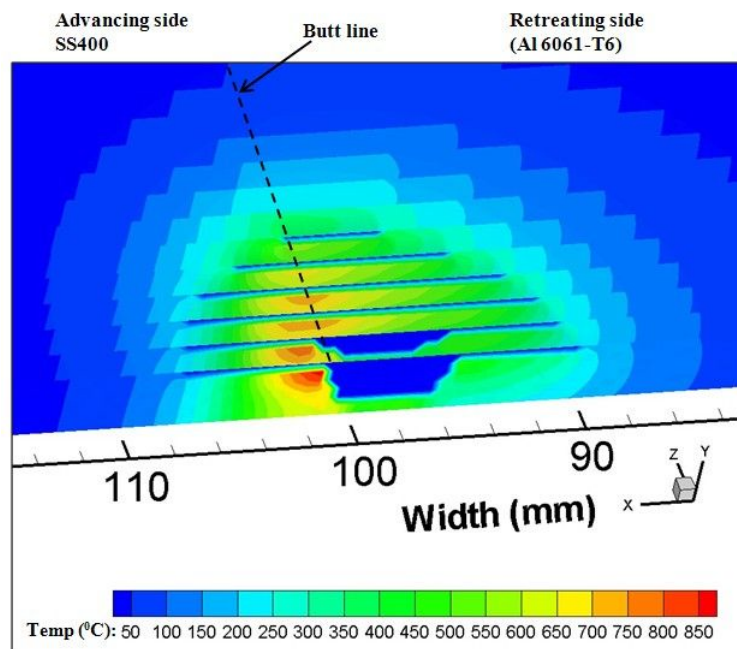
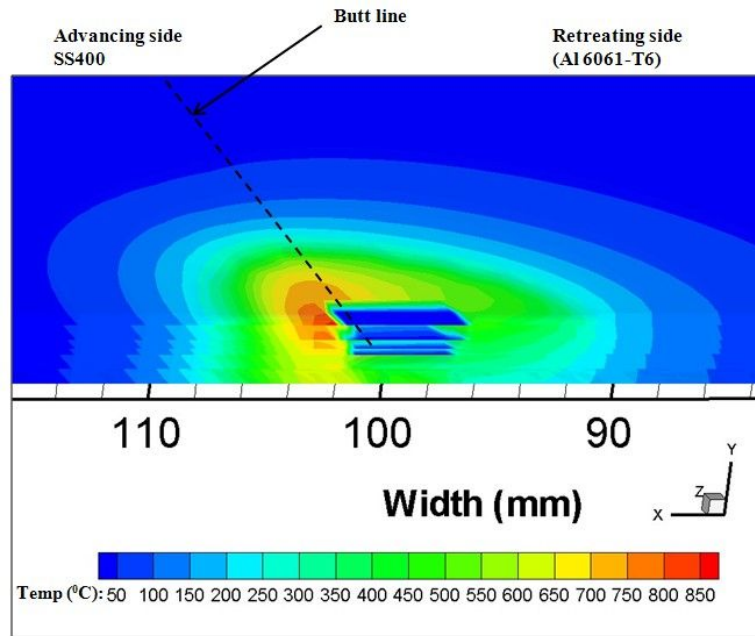
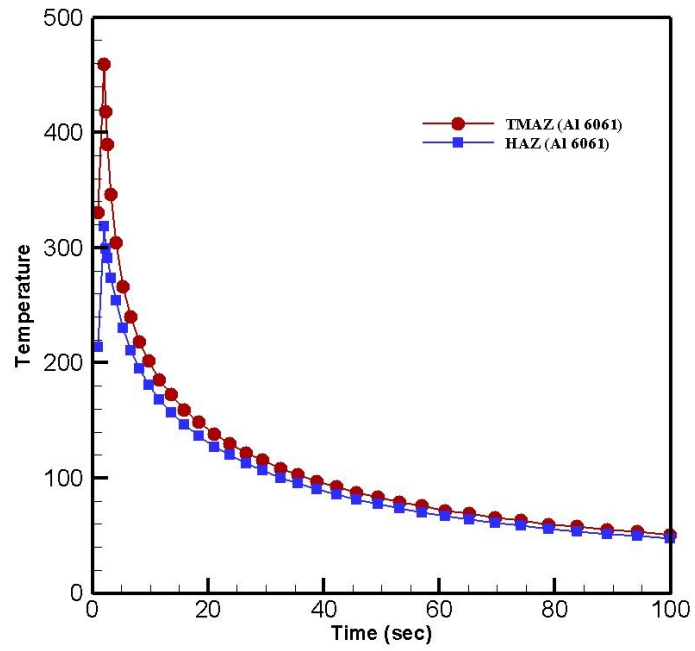
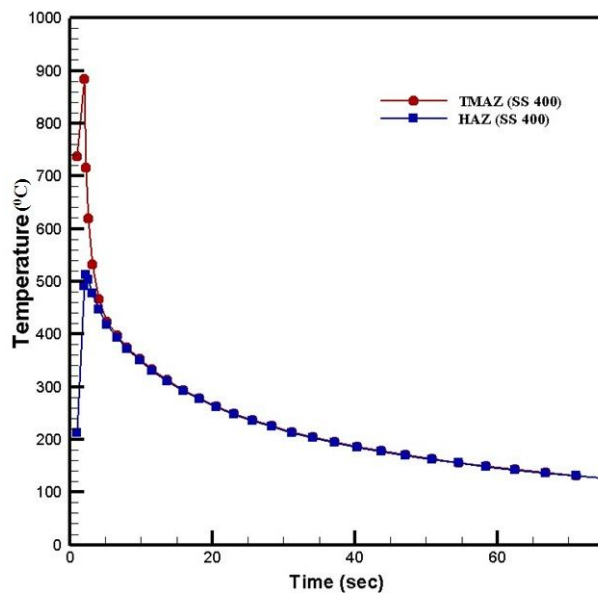


Fig. 5.4 Temperature contour along weld length and thickness obtained at 2sec for
Al6061-SS400 butt joint



(b) retreating side (Al6061-T6)



(b) advancing side (SS400)

Fig 5.5 Time-Temperature plot for Al 6061-SS400 dissimilar joint by TAFSW

5.2 Heat conduction analysis of TIG preheating

Heat conduction analysis of preheating TIG source is carried out as it has important role in estimating the temperature during TAFSW. TIG heat source is positioned at 20mm ahead of FSW tool center. The time for full traverse of the tool pin to form complete weld at a welding speed of 0.8mm/s and 300 rpm is 22.5 seconds for Al-STS304 joint. This time is 18 seconds for Al-SS400 joint produced at welding speed of 1.0mm/s and 300 rpm. The position of TIG electrode during and after welding is shown in Fig 5.4. The temperature contour obtained at 1 sec and between 18 and 22.5 sec is shown in Fig 5.5 and Fig 5.6. An inverse analysis is carried out to find the heat input required for the analysis of TAFSW.

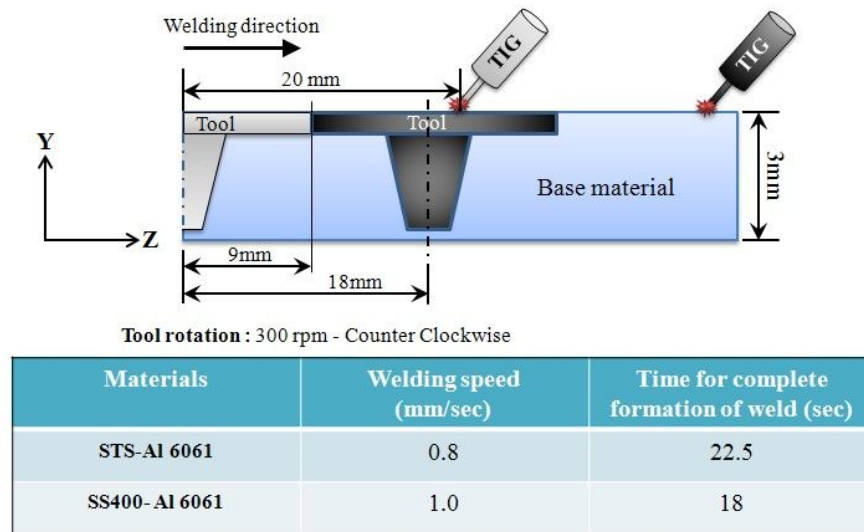


Fig 5.6 Location and time of TIG torch during and after welding

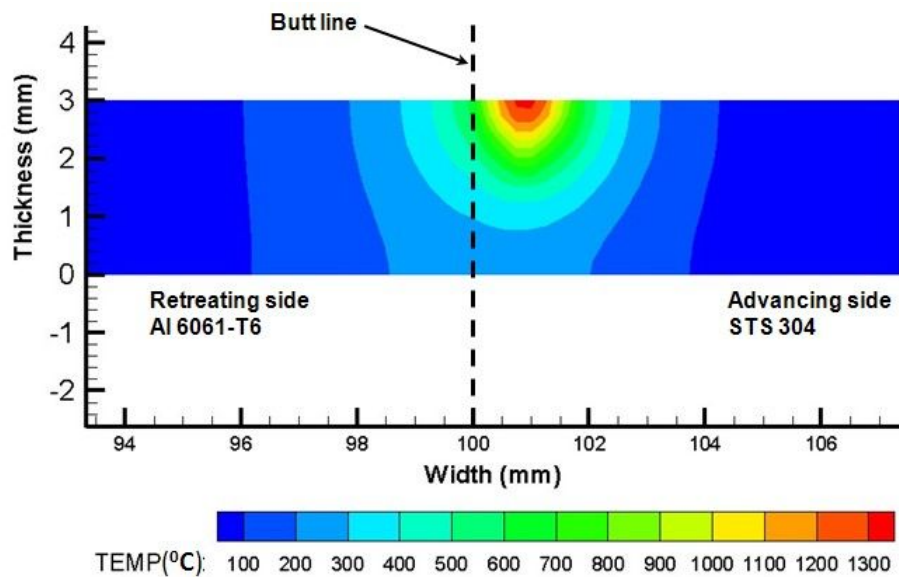
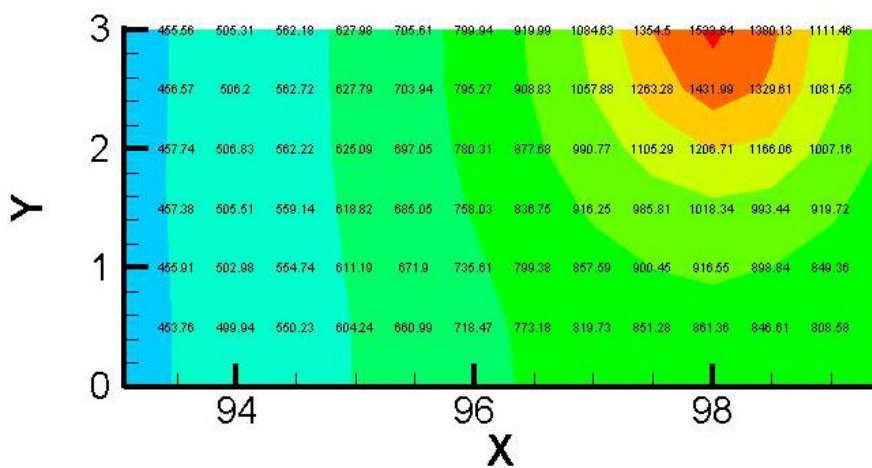
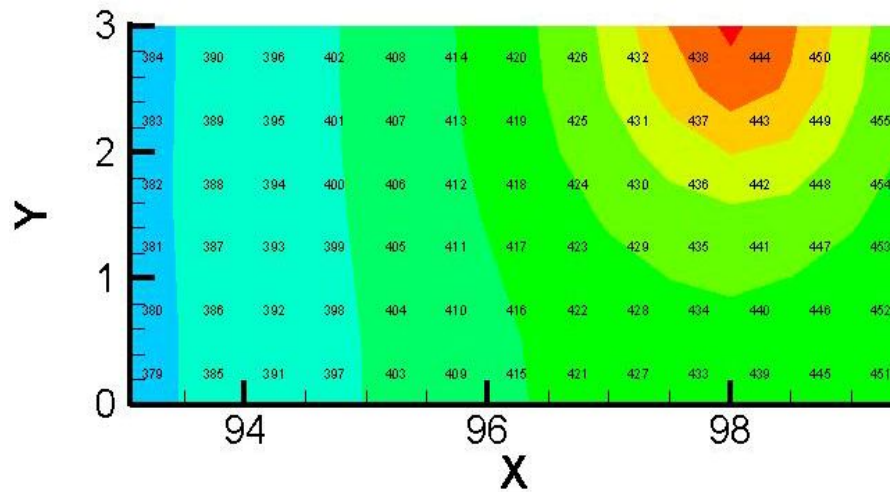


Fig 5.7 Temperature contour for TIG preheating obtained at 1sec



a) during welding



b) between 18-22 secs after welding

Fig 5.8 Temperature contour for TIG preheating during and after 20mm traverse

5.3 Analysis of dissimilar butt joint by Conventional FSW

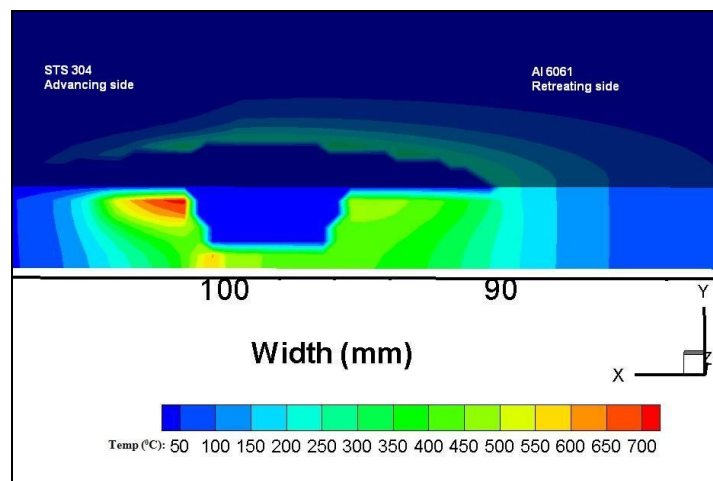


Fig. 5.9 Temperature contour along obtained at 2sec for Al6061-ST304 butt joint by conventional FSW

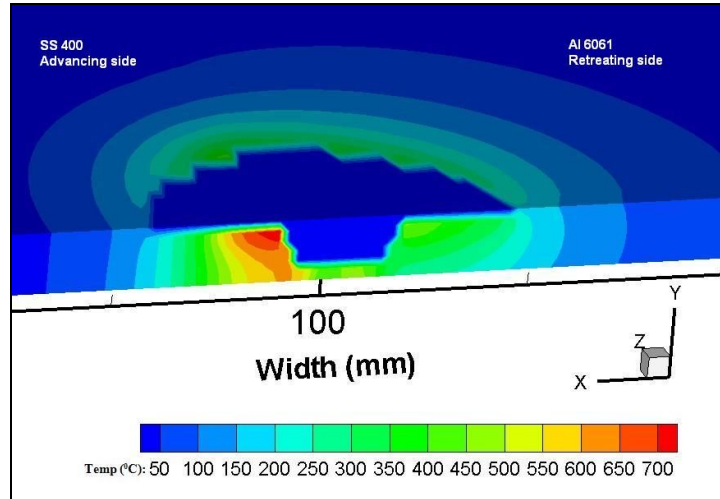


Fig. 5.10 Temperature contour obtained at 2sec for Al6061-SS400 butt joint by conventional FSW

The maximum temperature occurred in conventional FSW process is between 700-750⁰C in Aluminum- Steel joints. The temperature contour plots of Al-STS and Al-SS400 dissimilar joint is shown in Fig 5.9 and Fig 5.10 respectively. This change in temperature in TAFSW and FSW is attributed to preheating effect. The temperature flow pattern is almost similar other than a small variation in heat distribution along both retreating and advancing side. The heat distribution is wider in Aluminum alloy by TAFSW compared to FSW.

5.4 Residual stress analysis

Longitudinal and transverse residual stresses on weld region at distances 0.2 and 1.4mm below top surface is investigated for Al-STS304 and Al-SS400 dissimilar butt joint by numerical simulation. In most of the researches the residual stress occurred in FSW of similar materials reveals a typical “M-Like” profile [28] [34] [39].

It has been previously observed that residual stresses in similar joints by FSWs are lower relative to the base metal yield strength than those observed here [35][36]. This may be due to a number of factors enumerated previously for austenitic steels (e.g. coefficient of thermal expansion, thermal conductivity, and elevated temperature flow stress) or it may be caused by the more complex hardness/strength distribution observed in high strength aluminium alloy friction stir welds as compared to stainless steels that are welded in an annealed condition [37] [38]. In particular, it is observed that high strength aluminium alloy friction stir welds may be significantly under-matched rather than overmatched relative to the base metal and that the minimum strength region occurs in the HAZ. Hence, instead of the yield strength of the base metal limiting the residual stress, perhaps the yield strength of the relatively weak HAZ limits the residual stress level. If the 304 stainless steel were welded in a strain hardened condition, then one might expect that a relatively soft HAZ would develop and that this soft HAZ would then place a limit on the residual stress rather than the base metal.

The heat input during FSW is assumed to be caused by the friction between the tool shoulder and the sample surface. Thus, the heat generation is no longer concentrated within a narrow line as during fusion welding, but rather spread throughout a broad region having the width of the tool shoulder diameter. The strongest temperature gradients are not expected to be in the middle of the weld but at the edges of the shoulder. This area is characterized by the highest tangential speeds of the tool and, thus also by the highest heat production rates. The last regions cool down are therefore, those distance from the weld center directly under the tool shoulder edge. Hence the residual stress distribution after FSW can be imagined as a superposition of two single-peaked profiles, with each tensile residual stress maximum lying at one

edges of the tool shoulder. As a result, two tensile stress maxima appear symmetrically displaced with respect to the weld centerline. This is normal in the case of similar material joint by FSW.

5.4.1 Al 6061-STS 304 dissimilar joint

The rigid clamping used impedes the contraction of the weld nugget and heat-affected zone during cooling in both longitudinal and transverse directions and gives rise to residual stresses. In some circumstances compressive stresses can be beneficial, but tensile stresses can be detrimental to the welded structures as it can initiate crack propagation [54]. The residual stress distribution in dissimilar joint by TAFSW is obtained by applying heat input load calculated from heat conduction analysis to residual stress program. Longitudinal and transverse residual stress characteristics of Al 6061-STS304 dissimilar butt joint in the direction perpendicular to the welding line at distances 0.2 and 1.4mm below top surface and at distance -50 to 50mm along width is shown in Fig 5.4, Fig 5.5, Fig 5.6, and Fig 5.7 respectively. The residual stress characteristics during welding (with clamping) and after welding (clamping released) are presented here. In case of dissimilar materials, the difference in the material properties, rigid clamping, application of tool downward pressure, preheating effect and position of tool during TAFSW are responsible for a complex profile of residual stress distribution. The only way to predict residual stress by numerical simulation in dissimilar material joint by TAFSW is to input proper heat input load which is the body force applied to determine residual stress characteristics. Both condition of with clamp fixing and clam release is shown in figures. From the results, the residual stress distribution is found to be altered on releasing the fixtures after TAFSW. Generally, longitudinal residual stresses are compressive and tensile at mid regions near the tool shoulder edge of at Al 6061 and STS304. There is an increase in stress values after

cooling when the fixture is released. The stress distribution is tensile in longitudinal and transverse direction away from tool shoulder edge towards base materials. Except for the transverse stress distributions, there is no significant difference in the longitudinal stress distributions at both the distances from top surface. Large variances in transverse residual stresses are observed at distances 0.2mm and 1.4mm below top surface respectively. This indicates that temperature gradient exists throughout the thickness of the welded area.

It is observed that transversal residual stress is generally lower than longitudinal residual stress. The longitudinal stress values are increased when the fixture is released after welding. The longitudinal peak value of residual stress is close to each other at top surface in both aluminum and stainless steel side, at a distance corresponding to the edge of the tool shoulder. The difference in peak values between the two sides could easily be justified because of the higher yield strength of Al 6061, but it falls within measurement error. Residual stress in dissimilar thinner joints is very regular and always below 20 MPa in case of aluminium alloys dissimilar joints [31], and generally compressive both in longitudinal and transversal directions. But in STS304-Al6061 TAFSW joint peak value in longitudinal stress is lower than that in aluminum alloy side and localised in the STS304 side. This is because the stirring action took place mainly in the aluminium side because of the tool location with workpiece and steel alloys acts as a barrier for aluminium alloy to flow towards steel side during welding. Almost similar stress distribution along longitudinal direction is found at both depths, except for the transverse stress distribution at top surface. This is due to consideration of material removed from sheared surface by pin shoulder during welding. At STS304 side, localised longitudinal tensile and compressive stresses are observed. This might be due to plastic deformation and thus bonding between

dissimilar materials is expected to be stronger and assumed to extend half the specimen thickness due to the effect of preheating on STS304 surface. The residual stress at aluminum side is therefore subjected to tensile stress along certain distance and then becomes compressive. The maximum predicted longitudinal stress value at aluminum side and STS304 are approximately 12% and 15% of their respective material yield strengths. The rise in residual stress is about 20-35% after the clamping is released in both advancing and retreating sides.

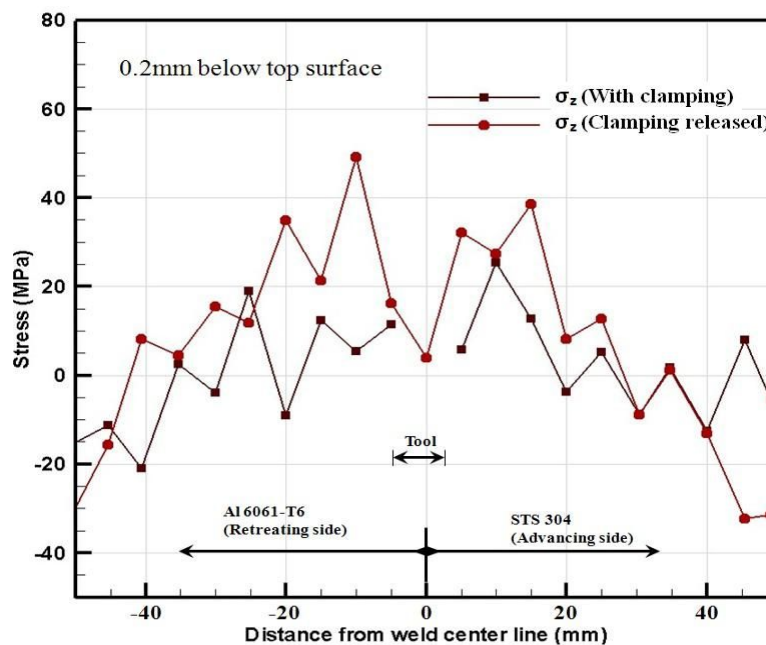


Fig 5.11 Longitudinal stress distribution at 0.2mm below top surface of Al6061-ST304 dissimilar joint

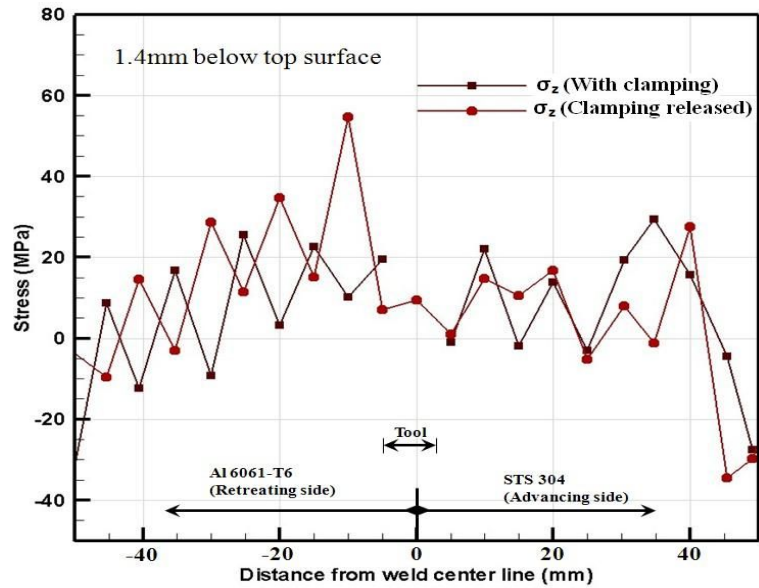


Fig 5.12 Longitudinal stress distribution at 1.4mm below top surface of Al6061-STs 304 dissimilar joint

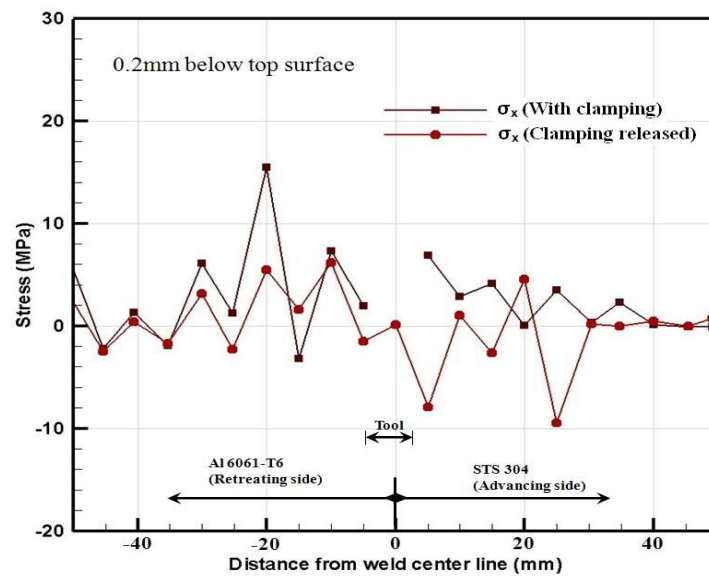


Fig 5.13 Transverse stress distribution at 0.2mm below top surface of Al6061-STs 304 dissimilar joint

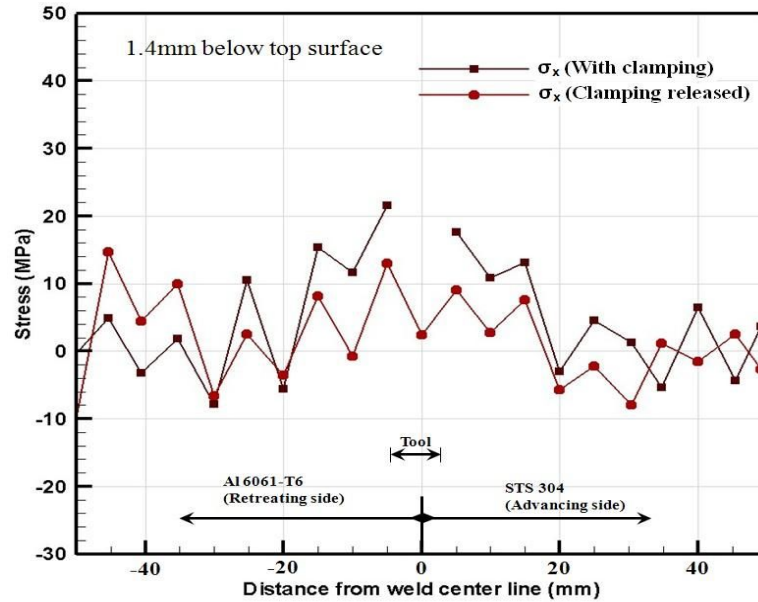


Fig 5.14 Transverse stress distribution at 1.4mm below top surface of Al6061-ST304 dissimilar joint

5.4.2 Al 6061-SS400 dissimilar joint

The residual stress distribution plot calculated at a depth of 0.2 and 0.4mm below top surface along longitudinal and transverse direction in Al 6061-ST304 dissimilar joint is shown in Fig 5.8, Fig 5.9, Fig 5.10, and Fig 5.11 respectively. As in the case of residual stress produced in Al-6061-ST304 dissimilar joint, the longitudinal residual stresses in AL 6061-SS400 dissimilar joint are primarily dominated by work piece's restraint (rigid clamping) in the longitudinal direction. The transverse residual stress distribution, however, can be attributed to both longitudinal and transverse restraints. During welding, heat is generated throughout a broad region having the width of the tool shoulder diameter. Therefore the residual stress produced was asymmetrical due to the asymmetry in the plasticized material volume along the advancing and retreating side of the stir zone that generated the heat. It is observed that longitudinal residual stresses at Al 6061 rises more than SS400 on relaxing the clamps after welding. This is because plastic deformation

occurred more at aluminum side than at steel side. Maximum stress is produced at SS400 below 0.2mm from top surface due to the effect of preheating. The residual stresses exhibit a compressive nature near the weld nugget where it is expected to be work hardened by the FSW tool and becomes tensile towards the base metal. But, at the center of weld, tensile stress is produced. The maximum longitudinal residual stress at Al6061 is 48.23MPa which is approximately 18% of aluminum base metal yield strength. The transverse stresses (σ_x) are characterized by tensile stresses at 0.2mm depth after the clamps are released. At 1.4mm depth the transverse residual stresses are compressive at weld center line. This suggests that a temperature gradient exists throughout the weld thickness. At preheated region in steel side, the transverse residual stresses are tensile at the mid region. An oscillatory nature of compressive and tensile residual stress distribution is observed in transverse direction. The longitudinal residual stress at Al6061 side near weld nugget zone during welding rise to about 55% at mid region when the clamps are released and this rise is about 15% at region away from the tool shoulder. At SS400 side the rise in longitudinal stress after the clamps are released is between 60-73% exhibiting stresses less compressive than aluminum. Some oscillations with rapid decrease and increase in stress values can be seen for some distance nearer to stir zone before the transverse component gradually approaches near to zero. As expected, the weld metal strength mismatch effects are most significant at the weld nugget region. The asymmetric behavior of residual stresses due to mismatch effects is expected to decrease rapidly as the distance from the weld centerline increases and outside of heat affected zone (HAZ), this asymmetry may become negligible for the cases studied.

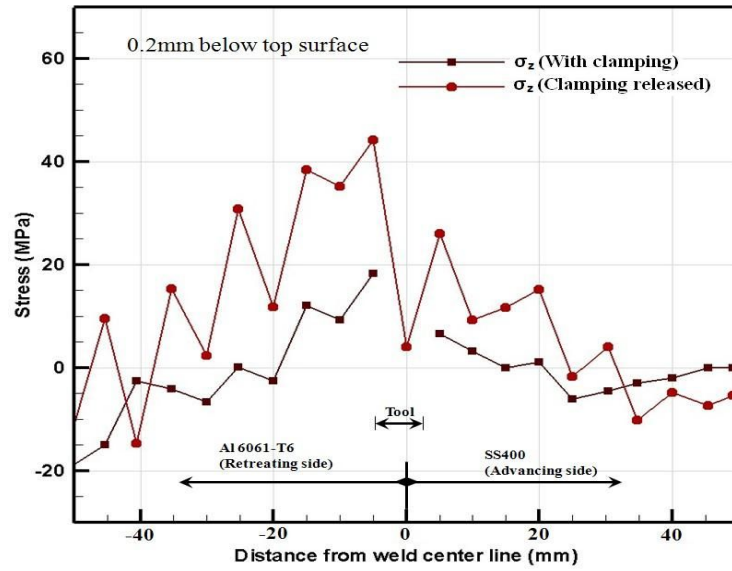


Fig 5.15 Longitudinal stress distribution at 0.2mm below top surface of Al6061-SS400
dissimilar joint

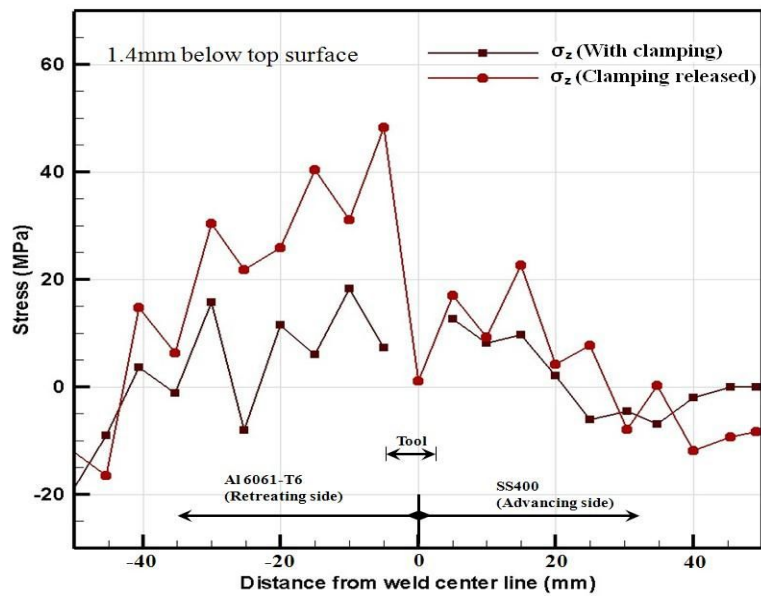


Fig 5.16 Longitudinal stress distribution at 1.4mm below top surface of Al6061-SS400
dissimilar joint

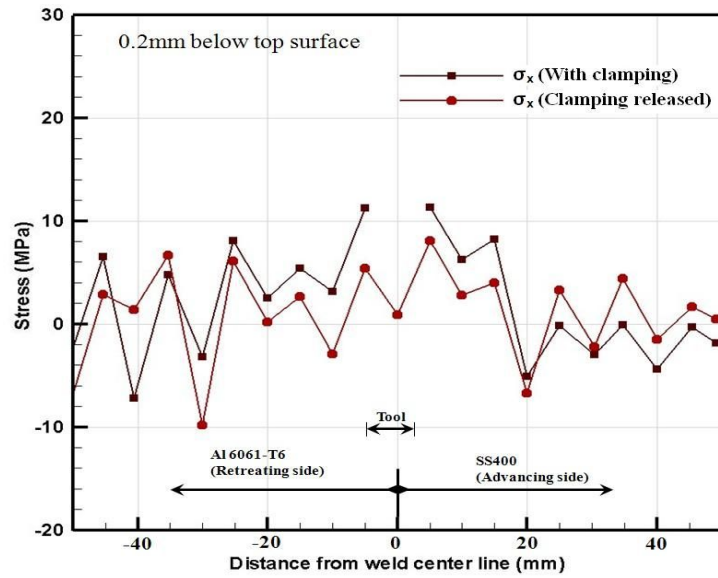


Fig 5.17 Transverse stress distribution at 0.2mm below top surface of Al6061-SS400
dissimilar joint

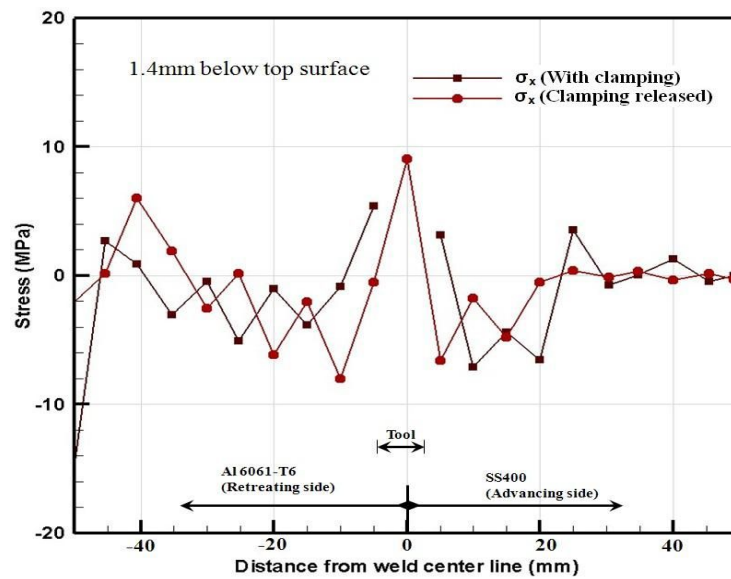
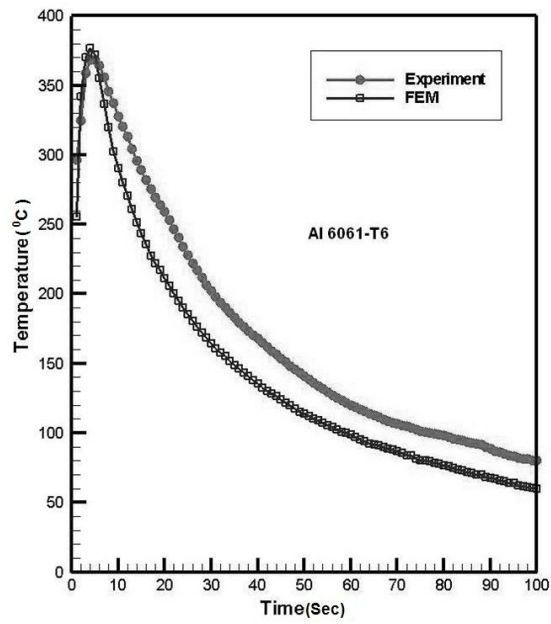


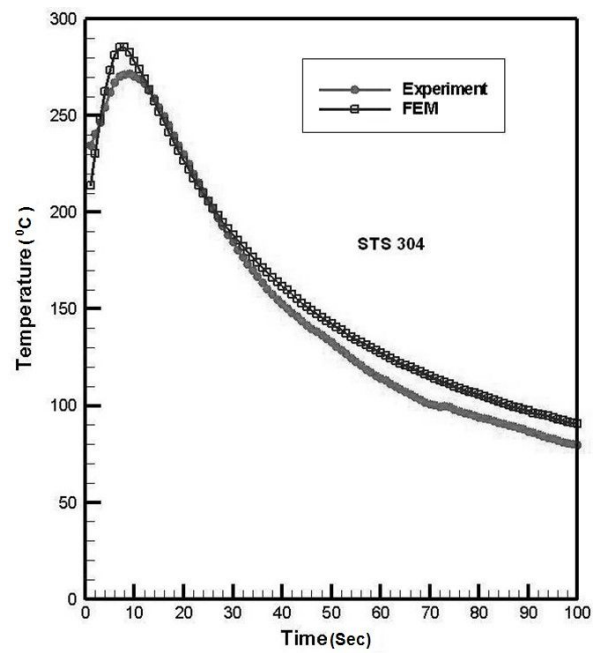
Fig 5.18 Transverse stress distribution at 1.4mm below top surface of Al6061-SS400
dissimilar joint

5.5 Comparison of numerical simulated and experimental result

In order to establish the feasibility of numerical simulation to dissimilar joints, the simulated results are compared with experimental results of Al 6061- STS304 and Al 6061-SS400 dissimilar joints respectively. Numerical simulation results are validated with experimental results obtained through infrared camera and thermocouples. Higher temperature distribution at STS304 surface is clearly visible from the infrared camera image. This instantaneous surface temperature measured on material-tool interface is compared with numerical simulation results and a reasonable match is observed. Fig 5.19(a) and Fig 5.19(b) shows the comparison at distances away from center line where the thermocouples are placed at retreating side (Al 6061) and advancing side (STS304/SS400). The measurement at equal distance from weld center could not be taken as the tool position is moved along aluminum material side and also, the temperature around the join line could not be measured as the travelling tool during welding obstructs measurement either by moving or damaging thermocouples.

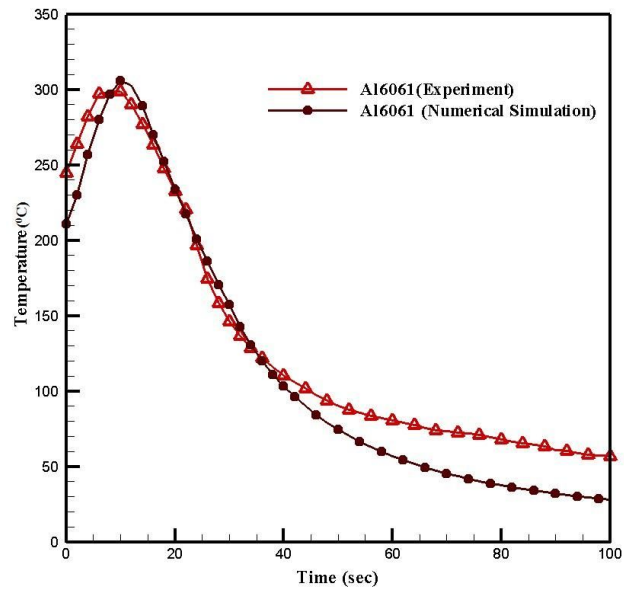


(12mm away from butt line)

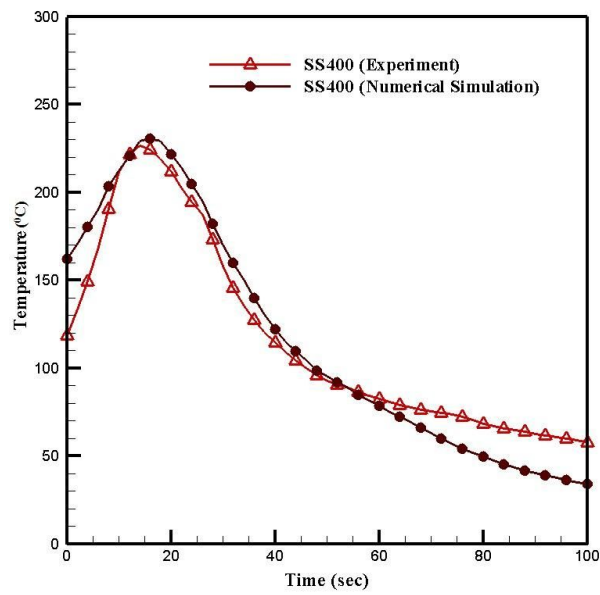


(9mm away from butt line)

a) Al6061-ST304 dissimilar joint



(14mm away from butt line)



(10mm away from butt line)

b) Al6061-SS400 dissimilar joint

Fig. 5.19 Comparison of numerically simulated and measured temperature history

The longitudinal residual stress values (σ_z) measured on Al6061 and STS304 dissimilar joint at 8 different locations are compared with numerical simulation results (Fig.20). The difference in the values may be due to change in material dimensions, type of fixity (clamping), errors in measurement, etc.

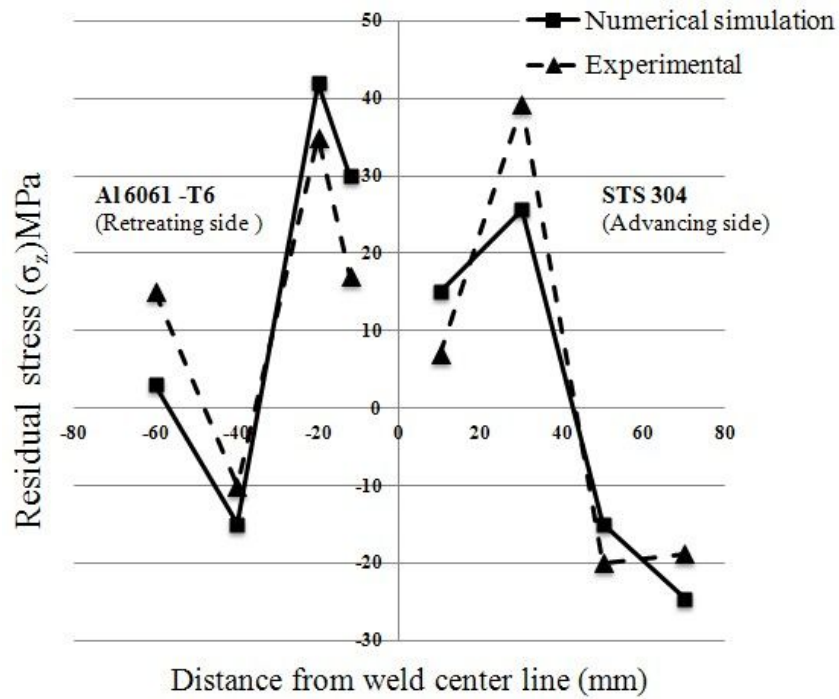


Fig. 5.20 Comparison of experimentally measured and numerically simulated values of longitudinal residual stress (σ_z) at top surface of Al6061-ST304 welded specimen

Chapter 6

CONCLUSION AND FUTURE SCOPE OF WORK

Friction stir welding has immensely high potential in the field of thermo mechanical processing of various alloys extending from similar to dissimilar joints, especially aluminum to high strength steels. This thesis presents numerical determination of temperature and residual stress characteristics of TIG assisted friction stir welding of Al 6061 and STS304/SS400 dissimilar butt joint. The heat distribution pattern and temperature history of Al 6061-ST304 and Al 6061-SS400 were presented respectively. The Residual stresses of both these joints were investigated by thermo-elasto plastic analysis and were presented. Also, the numerical and experimental results obtained have shown a reasonable good agreement. From the present numerical investigation the following conclusions are derived:

- The analytical model can be used to carry out the analysis of heat conduction, heat transfer and thermal elasto-plasticity in areas near the middle of dissimilar welding, assuming it is in a quasi-stationary state.
- The analytical model is strengthened by introducing slip factor and coefficient of friction, that partition the heat generation between plastic deformation and friction.
- The model, however, does not take into account heat generation from plastic deformation more precisely; therefore, the predicted temperatures in weld nugget region may decrease more rapidly than experimentally observed.
- The optimum parameters for TAFSW process of Al 6061 and STS304/SS400 dissimilar butt joint were obtained from experiment and

summarized in Table 4.3. The accuracy of the optimal solutions was evaluated by the results obtained from finite element analysis for particular work piece and tool geometry.

- Though the instantaneous maximum temperature is occurred near the tool pin, it is expected that heat generation is spread throughout the broad region having the width of the tool shoulder diameter.
- The strongest temperature gradients are expected at areas characterized by the highest tangential speeds of the tool. Therefore, it can be inferred that the last region to cool down are at regions directly under the tool shoulder edge.
- In Al 6061-STS304 butt joint, plastic deformation at STS304 side is expected to be stronger and assumed to extend half the specimen thickness. This could be because of its plastic state induced primarily by TIG pre-heating temperature.
- Aluminum alloy is completely made to deform plastically by stirring action of the pin and made to bond with steel which is frictionally heated. STS 304 acts a barrier for aluminum material to flow towards steel during welding; however, this phenomenon is less in Al6061-SS400 butt joint. Hence the TMAZ of aluminum is more in butt welded joint with steel compared to FSW joints of similar aluminum alloys.
- Due to reduction in material area below tool pin, more heat is conducted at pin bottom than at pin sidewalls. Aluminum conducts heat more at this contact region and slightly tends to melt at the butt joint surface.
- The computed temperature history in each node from the thermal analysis is input as body load to determine residual stress distribution of dissimilar

aluminum-steel joint. The peak value in longitudinal stress is lower than that in aluminum alloy side and localised in the steel side. This is due to the preheating effect by TIG torch on STS304/SS400 surface.

- The longitudinal residual stress in Al 6061-STSS304 joint is highly tensile at top surface and middle region. Along transverse line both tensile and compression is exhibited. In Al6061-SS400 dissimilar joint, Only top surface longitudinal stress are tensile in nature, where as the longitudinal and transverse residual stress are oscillate between states of compression and tension.
- The maximum predicted longitudinal stress value at Al 6061-T6 and STSS304 were approximately between 12-15% of their respective material yield strengths. This value is about 20% yield strength of aluminum base metal in Al 6061 and SS400 dissimilar joint.
- Also, complemented advantage of preheating eases out the process of FSW reducing the required torque due to lower friction.
- The residual stress values, in Al 6061-STSS304, during welding (with clamping) are increased to about 20-35% after welding when the clamping are released in both advancing and retreating sides. This rise in values are about 28-40% in Al 6061-SS400 dissimilar joint.
- Furthermore, very good agreement between the simulated and measured temperature shows the credibility of the heat conduction model used and developed, potentially providing inputs for various simulations, such as residual stress formation mechanism and distortion of the weldment.

- With this numerical model established, results can be taken into various cases of temperature predictions in dissimilar materials, predominantly for steel to aluminum joints.

6.1 Future scope of work

While it was beyond the scope of the current research to provide a detailed study of the analytical model for dissimilar Aluminium – Steel butt joint by TAFSW presented here, the detail provided herein should serve as a stepping stone in future research works stated below:

- The research could be taken further by applying the same technique to other dissimilar joints of Aluminum alloys such as 5XXX and 7XXX with Magnesium, Copper, Titanium etc., which are the alloys used in the automotive industry. This could help the increase of use of the friction stir welding in the automotive industry.
- Further investigations on the forces generated during single and multiple passes for different alloys at different conditions and for different process parameters might be very beneficial.
- The heat and thermo elastic plastic analysis with this model can more precisely be done considered the intermetallic compounds and its temperature dependency to the analytical equations when analyzing dissimilar welded joint of materials having entirely different material properties.
- The heat flow analysis with tool and backing plate has to be conducted in order to understand the accurate thermo mechanical behavior of dissimilar joints.

REFERENCES

- [1] Scott Brown, Feasibility of Replacing Structural Steel with Aluminum Alloys in the Shipbuilding Industry; (1999),
<http://tc.engr.wisc.edu/uer/uer99/author1/index.html>.
- [2] Dawes. C.J, Thomas W.M., Friction Stir Process *Welds* Aluminum alloys, *Weld. J.* **75** (1996), pp.41-46.
- [3] R.S.Misra, Z.Y.Ma, Friction Stir Welding and Processing, *Mater. Sci. Eng. R* **50** (2005), pp. 1-78.
- [4] M. P. Miles, T. W. Nelson, D. W. Melton, Formability of friction-stir-welded dissimilar-aluminum-alloy sheets, *Metall. Mater. Trans. A* **36A** (2005), pp. 3335-3342.
- [5] W.B.Lee, M. Schmuecker, U.A. Mercardo, G.Biallas, S.B. Jung, Interface reaction in steel–aluminum joints made by friction stir welding, *Scripta Mater.***55** (2006), pp. 355–358.
- [6] H.Uzun, C.D.Donne, A.Argagnotto, Friction stir welding of dissimilar. Al 6013-T4 To X5CrNi18-10 Stainless Steel, *Mater. Design* **26** (2005), pp. 41-46.
- [7] Thaiping Chen, Process parameters study on FSW joint of dissimilar metals for aluminum–steel, *J Mater Sci* **44** (2009), pp. 2573–2580.
- [8] H. Okamura. K. Aota, Joining of dissimilar materials with friction stir welding, *Weld Int*, **11** (2004), pp.852 – 860.
- [9] W.H.Jiang, R.Kovacevic, Feasibility study of friction stir welding of 6061-T6 aluminium alloy with AISI 1018 steel, *J. Eng Manuf.* **10** (2004), pp.1323-1331.

- [10] G.Kohn, Y.Greenberg, I.Makover, A.Munitz, Laser-assisted friction stir welding, *Welding J* **81** (2002), pp. 46-48.
- [11] <http://www.twi.co.uk/content/fswintro.html>
- [12] Thaiping Chen, Process parameters study on FSW joint of dissimilar metals for aluminum–steel, *J Mater Sci* **44** (2009), pp. 2573–2580.
- [13] Gould. J.E. and Feng. Z.L., *Heat flow model for friction stir welding of aluminum alloys* *Journal of Materials Processing & Manufacturing Science*, 1999. **7**(2): pp. 185-194.
- [14] Chao. Y.J, Qi. X., and Tang. W., *Heat transfer in friction stir welding - Experimental and numerical studies*, *Journal of Manufacturing Science and Engineering-Transactions of the ASME*, 2003. **125**(1): pp. 138-145.
- [15] Colegrove P, *3 Dimensional flow and thermal modeling of the Friction Stir Welding process*, in: the Second FSW Symposium, Gothenburg, Sweden, 2000.
- [16] Khandkar. M.Z.H, Khan. J.A., and Reynolds A.P, *Prediction of temperature distribution and thermal history during friction stir welding: input torque based model*, *Science and Technology of Welding and Joining*, 2003. **8**(3): pp. 165-174.
- [17] Song. M. and Kovacevic. R., *Heat transfer modelling for both workpiece and tool in the friction stir welding process: a coupled model*. *Proceedings of the Institution of Mechanical Engineers Part B-Journal of Engineering Manufacture*, 2004. **218**(1): pp. 17-33.
- [18] Vilaca. P, Quintino. L and dos Santos, J.F., *iSTIR - Analytical thermal model for friction stir welding*. *Journal of Materials Processing Technology*, 2005. **169**(3): pp. 452-465.

- [19] Chao. Y.J. and Qi. X.H, *Thermal and thermo-mechanical modeling of friction stir welding of aluminum alloy 6061-T6*. *Journal of Materials Processing & Manufacturing Science*, 1998. **7**(2): pp. 215-233.
- [20] Chen. C.M. and Kovacevic. R, *Finite element modeling of friction stir welding - thermal and thermomechanical analysis*. *International Journal of Machine Tools & Manufacture*, 2003. **43**(13): pp. 1319-1326
- [21] Zhu. X.K. and Chao. Y.J, *Numerical simulation of transient temperature and residual stresses in friction stir welding of 304L stainless steel*, *Journal of Materials Processing Technology*, 2004. **146**(2): pp. 263-272.
- [22] Soundararajan. V, Zekovic. S and Kovacevic. R., *Thermo-mechanical model with adaptive boundary conditions for friction stir welding of Al 6061*. *International Journal of Machine Tools & Manufacture*, 2005. **45**(14), pp. 1577-1587.
- [23] Khandkar. M.Z.H, Khan. J.A., Reynolds. A.P and Sutton. M.A, *Predicting residual thermal stresses in friction stir welded metals*. *Journal of Materials Processing Technology*, 2006. **174**(1-3): pp. 195-203.
- [24] Nandan. R., Roy. G.G. and Debroy. T, "Numerical Simulation of Three-Dimensional Heat Transfer and Plastic Flow during Friction Stir Welding" 2006, *Metallurgical and Materials Transactions A*, **37A**, pp.1248-1259.
- [25] K. Li. D. Aidun, and P. Marzocca, 3-D Thermo-Mechanical Analysis of Friction Stir Welding of Dissimilar Metals Using Functionally Graded Material Concept, *Trends in Welding Research, Proceedings of the 8th International Conference*, pp. 726-730.

- [26] Shmidt. H, Hattel. J. and Wert. J, An analytical model for the heat generation in friction stir welding, *Modeling and Simulation in Materials Science and Engineering*, **12**, 2004, pp.143–157.
- [27] Colligan. K, 1999, *Welding Journal*, **6**, pp. 229 –237.
- [28] Colegrove P, 2000, *2nd Int. Symp. on Friction Stir Welding (Gothenburg, Sweden)*
- [29] S.R. Rajesh, H.S. Bang, H.J. Kim, H.S. Bang, Analysis of complex heat flow phenomena with friction stir welding using 3D-analytical model, *Adv. Mats Res*, **15-17** (2007) pp. 339–344.
- [30] Yukio Ueda, You Chul Kim, Teruhisa Yamakita and Han Sur Bang, *J. Jap. Wel. Soc.* **6** (1988) (1) pp. 47-53.
- [31] JAHM, 2003 Material Properties Database, Copyright © 2003 JAHM Software, Inc,USA.
- [32] V. Dattoma, M. De Giorgi and R. Nobile On the Residual Stress Field in the Aluminium Alloy FSW Joints, *Strain* (2009) **45**,pp. 380–386
- [33] H Schmidt, J Hattel, Modelling heat flow around tool probe in friction stir welding, *Sci. Technol. Weld. Joining* **10** (2005) (2), pp.176-186.
- [34] J H Hattel, HNB Schmidt and C.Tutum, Thermomechanical Modelling of Friction Stir Welding, *Proc of the 8th Int Conf.*, Georgia, USA (2008), pp. 1-10.
- [35] Numerical simulation thermal history and residual stress in FSW of Al2014-T6, N.Rajamanickam, V.Balusamy, P.R.Thyla and G.hari Vignesh, *Journal of scientific and industrial research*, Vol 68, March 2009, pp. 192-198.
- [36] Sutton MA, Reynolds AP, Wang DQ, Hubbard CR, *J Eng Mater Tech*, 2002, pp.124-215.

- [37] James M, Mahoney M, Waldron D. *Proceedings of the 1st ISFSW*, 1999, California, USA.
- [38] Kroninger. H. and Reynolds. A., “R-Curve Behavior of Friction Stir Welding in Aluminum-Lithium Alloy 2195”, *Fatigue and Fracture of Engineering Materials and Structures*, Vol. 25, pp. 283-290, 2002.
- [39] Lockwood. W. D, Tomaz. B and Reynolds. A.P 2002 Mechanical response of friction stir welded AA2024: experiment and modeling *Mater. Sci. Eng. A* **323**, pp. 348–53
- [40] A.P. Reynolds, Wei Tang , T. Gnaupel-Herold , H. Prask, Structure, properties, and residual stress of 304L stainless steel friction stir welds, *Scripta Mater*, **48** (2003) 1289–1294.
- [41] Yukio UEDA and Taketo YAMAKAWA. “Analysis of Thermal Elastic-Plastic Stress and Strain during Welding by Finite Element Method.” *Transaction of the Japan Welding Society*, Vol. 2, No. 2, September 1971, pp.90-100.
- [42] Cavaliere. P, Dattoma. V and Panella. F.W., Numerical analysis of multipoint CDW welding process on stainless AISI304 steel bars, *Computational Material Science*, vol.46, 2009, pp. 1109-1118.
- [43] Nandan. R, Roy. G. G, Lienert T. J, and DebRoy T., Numerical modelling of 3D plastic flow and heat transfer during friction stir welding of stainless steel, *Science and Technology of Welding and Joining*, vol.1, 2006, pp. 526-537.
- [44] Chen. Y, Li. L, Fang. J and Feng, X., Numerical Analysis of Energy Effect in Laser-TIG Hybrid Welding, *Journal of Materials Science & Technology*, vol.19, pp. 23-26, 2003.
- [45] Giridharan P. K and Murugan. N., Optimization of pulsed GTA welding process parameters, *Int J Adv Manuf Technol*, **40** (2009) pp.478–489.

- [46] Song, M., and Kovacevic, R., 2003, "Numerical and Experimental Study of the Heat Transfer Process in Friction Stir Welding", *Proc. Instn Mech. Engrs*, vol. 217, pp. 73-85.
- [47] Xu, S., Deng, X., Reynolds, P., and Seidel, T., 2001, "Finite Element Simulation of Material Flow in Friction Stir Welding", *Science and Technology of Welding and Joining*, vol. 6, pp. 191-193.
- [48] Schmidt, H., and Hattel, J., 2005, "A Local Model for the Thermomechanical Conditions in Friction Stir Welding", *Modelling and Simulation in Material Science and Engineering*, pp. 77-93.
- [49] Song, M., Kovacevic, R., Ouyang, J., and Valant, M., 2002, "A Detailed Three-Dimensional Transient Heat Transfer Model for Friction Stir Welding", *Proceeding of the 6th International Trends in Welding Research Conference*, Pine Mountain, GA.
- [50] Frigaard, Ø., Grong, Ø., and Midling, O., 1998 "Modelling of Heat Flow Phenomena in Friction Stir Welding of Aluminum Alloys", *Proceeding of the 7th International Conference on Joints in Aluminum*, Cambridge, UK.
- [51] Awang, M., Mucino, V. H., Feng, Z., and David, S. A. (2005). "Thermo-mechanical modeling of friction stir spot welding (FSSW) process: Use of an explicit adaptive meshing scheme." *SAE 2005 World Congress*.
- [52] K.H.Park, Development and analysis of ultrasonic assisted friction stir welding process, PhD Thesis (2009), The University of Michigan.
- [53] Koichi Masubuchi, Analysis of Welded Structure, PERGAMON PRESS, pp.1~234, 1980

- [54] J Goldak, Aditya Chakravarti, and M Bibby. "A New Finite Element Model for Welding Heat Sources." *Metallurgical and Materials Transactions B*, **15B**, pp.299~305, June 1984.
- [55] Rodrigo S. Coelho, Aleksander Kostka, Jorge F. dos Santos and Anke R. Pyzalla, EBSD Technique Visualization of Material Flow in Aluminum to Steel Friction-Stir Dissimilar Welding, *Advanced Engineering Materials* 2008, 10, No. 12.

ABSTRACT

Development of analytical model for Thermo-mechanical behavior of dissimilar materials butt joint by TIG Assisted Friction Stir Welding

M.S.Bijoy

Advisor: Prof. Bang Han Sur, Ph.D.

Department of Naval Architecture
and Ocean Engineering

Graduate School of Chosun University

When joining aluminium to steel, equipment rigidity, high force to move the tool and high tool wear rate during FSW induces weld defects. These drawbacks can be overcome by localised preheating the surface of harder material ahead of the rotating tool pin during FSW process. A volume of the material plasticizes during preheating and further to this the welding process can be carried out in the same way as conventional FSW. In this study TIG heat source is used to preheat the harder material (STS 304/SS400) in order to make a sound weld joint with Aluminum alloy (Al 6061-T6). Three-Dimensional heat conduction analysis on dissimilar joint by TIG Assisted FSW (TAFSW) is carried out using an analytical model to determine the thermal histories and the temperature distribution that helps in successful implementation of TAFSW to dissimilar materials and helps in predicting residual stress and weld strength. Therefore, this study intends to gain a clear physical insight of thermal history and temperature distribution in dissimilar butt joint between aluminum alloy (Al 6061-T6) and steel (STS 304/SS400) using TAFSW.). For this, an analytical model to

determine the heat generation from tool surface during FSW process has been developed. In-house solver is used for finding the temperature distribution due to heat generation during TAFSW on dissimilar materials joint. The temperature load is applied as a body force in order to determine the residual stress characteristics using develop program. Residual stress characteristics during welding (with clamping) and after welding (when the clamps are released) are presented here. Moving heat source along with frictional heat between the work specimens and tool surface is considered for calculating the heat input. The analytical tool used predicts successfully the maximum welding temperatures that occur on the dissimilar materials during TAFSW.

Preheating due to TIG supplements the formation of plasticized state of stainless steel thereby enhancing the welding with aluminum alloy. During welding, the highest temperature is observed just below the shoulder near stir zone. The material flow is observed to be restricted towards stainless steel due to its material property difference. Complemented advantage of preheating eases out the process of FSW reducing the required torque due to lower friction. In dissimilar joint produced by TAFSW, the residual stress distribution was asymmetric with respect to the weld axis. In Steel-Al6061 dissimilar butt joint by TAFSW joint, peak value in longitudinal stress is lower than that in aluminum alloy side and localised in the Steel side. This is because the stirring action took place mainly in the aluminium side because of the tool location with workpiece and Stainless steel acts as a barrier for aluminium alloy to flow towards steel side during welding. Furthermore, very good agreement between the simulated and measured temperature shows the credibility of the heat conduction model used and developed, potentially providing inputs for various simulations, such as residual stress formation mechanism and distortion of the weldment. With this numerical model established, results can be taken into various cases of temperature and residual stress

predictions in dissimilar materials, predominantly for steel to aluminum joints. The application possibility of TIG assisted Friction Stir Welding to heavy industries has been established by this research work.

Acknowledgements

With immense gratitude, I would like to thank everyone who has been helpful in the successful completion of my Ph.D. study.

It is a great pleasure to express my hearty gratitude to my esteemed supervisor, **Professor Bang Han Sur** at Chosun University for giving his healthy suggestions, constant encouragement, kind guidance, support and care throughout this study. It has been a great opportunity to be part of his team and to work on an exciting topic with a lot of scientific freedom which helped me to complete this Ph.D course successfully. Without his unlimited supply of ideas and tips for solving problems and help in formulating the problems in the first place, the present work could not have taken shape.

It is an honor for me to thank my co-supervisor **Professor Bang Hee Seon**. Her valuable comments, understanding, encouragement and guidance have provided a good basis for the present thesis.

I wish to express my gratitude to all other Professors in the Department of Naval Architecture, Chosun University, for their encouragement and support in various ways.

I would like to express my special thanks to **Dr. C.G. Nandakumar**, Department of Ship Technology, Cochin University of Science and Technology, without whom my PhD course in Korea would never have happened.

Special thanks to my senior **Dr. Rajesh.S.R** who continuously supported me during my course work.

Thanks also to my lab mates especially, Mr.Son ChangSik, Mr.Jeon GeunHong, Mr. Kim JunHyung, Mr. Kwon YoungHyok, Mr. Beak JungYoun and others to be my friends, best colleagues and to create a good atmosphere in all the ups and downs during my Ph.D. career.

I extend my thanks to Korean teachers, the people in the International office, especially Mr. Son Ohki and the staffs of Graduate school at Chosun University for their great help.

On a personal level, I would like to thank my parents, my sister, my wife and my family members for their continuous support on my choices, their encouragement and love throughout my academic career. I fondly remember my late father, whose unfailing efforts and guidance which facilitated me to pursue my studies till Ph.D. I convey my thanks to all my Indian friends, especially Mr. Sandeep Nair, and others whom I cannot possibly name individually for their valuable support directly or indirectly and their timely help for the completion of this work.

My humble thanks to the almighty God for his everlasting guidance and love.